

High-order finite-volume integration schemes for subsonic magnetohydrodynamics

J.-M. Teissier¹ and W.-C. Müller^{1,2}

jm.teissier@astro.physik.tu-berlin.de

June 19, 2023

Abstract

We present an efficient dimension-by-dimension finite-volume method which solves the adiabatic magnetohydrodynamics equations at high discretization order, using the constrained-transport approach on Cartesian grids. Results are presented up to tenth order of accuracy. This method requires only one reconstructed value per face for each computational cell. A passage through high-order point values leads to a modest growth of computational cost with increasing discretization order. At a given resolution, these high-order schemes present significantly less numerical dissipation than commonly employed lower-order approaches. Thus, results of comparable accuracy are achievable at a substantially coarser resolution, yielding overall performance gains. We also present a way to include physical dissipative terms: viscosity, magnetic diffusivity and cooling functions, respecting the finite-volume and constrained-transport frameworks.

Keywords: Partial Differential Equations, Finite-volume schemes, High-order methods, Fluid Dynamics, Magneto-hydrodynamics, Turbulence

1 Introduction

Turbulence is an ubiquitous phenomenon in nature which still lacks a comprehensive theory. Progress in its understanding can be achieved by direct numerical simulation (DNS) of the Navier-Stokes equations (NSE) for neutral fluids. For electrically conductive media, such as liquid planetary cores or plasmas, ionized gases, found in many astrophysical environments, the equations of magnetohydrodynamics (MHD) are a convenient single-fluid description. This approximation is valid on large spatial and long temporal scales as compared to the microscopic characteristics of electric and magnetic interactions between the charged constituents. Therefore, MHD is widely used when dealing with geo- and astrophysical problems.

In natural systems, the Reynolds number Re , which characterizes the spectral bandwidth of turbulent fluctuations, can be orders of magnitude above the maximum values achievable by DNS on today's high-performance computing facilities. A main culprit limiting the achievable Reynolds number in DNS is insufficient numerical resolution of space and time and the consequential dissipation introduced via the numerical integration scheme and resulting in amplitude and phase errors of the numerical solution. Numerical dissipation is generated by the loss of information due to discretization errors, which is dominant at small scales and represents a lower bound on the physical dissipation one can apply in DNS via corresponding terms in the underlying differential equations.

A reduction of algorithmic numerical dissipation directly increases the spectral bandwidth of a DNS at the same numerical resolution, and ideally leads to more accurate numerical experiments at affordable computational cost. For this aim, more accurate Riemann solvers, which numerically approximate the time evolution of two neighbouring fluid states, have been developed [1, 2, 3, 4, 5, 6]. Another approach is to raise the discretization order, i.e. to go beyond the standard second-order approach by including terms of higher order in the Taylor expansion of the solution (assumed to be analytic within each computational cell). Even though at a given resolution higher-order discretization is computationally more demanding, such schemes can lead to a large gain in efficiency overall. Indeed, higher-order solvers typically require a lower resolution to reach a similar accuracy as compared to second-order schemes [7].

¹Technische Universität Berlin, ER 3-2, Hardenbergstr. 36a, D-10623 Berlin, Germany

²Max-Planck/Princeton Center for Plasma Physics

However, multi-dimensional polynomial reconstruction becomes increasingly expensive with a growing order of accuracy. A specific strategy to alleviate this problem is realized in “dimension-by-dimension” solvers. Instead of solving an expensive 3D reconstruction problem at once, they solve three one-dimensional cost-effective problems separately. A further gain in performance is achieved by a dimension-by-dimension approach which requires only one high-order reconstruction along each dimension [8, 9]. It relies on a transformation of reconstructed area-averages to high-order point values in the middle of the faces, from which high-order point fluxes are obtained that lead to high-order area averages.

The present work employs this numerical technique. It extends a dimension-by-dimension fourth-order finite-volume solver for the compressible MHD equations using the constrained-transport approach [7] up to order ten. The schemes are based on Weighted Essentially Non-Oscillatory (WENO) 1D reconstructions, associated with a passage through point values. Volume/area/line-averages \leftrightarrow point value transformations are derived using the method described in [8, 9].

Only subsonic flows are considered in this work. For supersonic flows, where shocks and discontinuities are prevalent, avoiding the generation of spurious oscillations near sharp gradients is a very challenging issue [10, 7, 11, 12] which we do not consider here. Our aim in this work is to provide a relatively simple framework to build computationally efficient higher-order 3D compressible MHD solvers.

The rest of this paper is organized as follows: section 2 describes the MHD equations to be solved as well as the chosen discretization (finite-volume in a Cartesian domain and constrained-transport for the magnetic field). Section 3 presents how the higher-order numerical schemes are built. Their numerical accuracy is verified in section 4 through convergence tests. That section presents as well an application example: driven turbulence in a statistically stationary state. Finally, concluding remarks are given in section 5.

2 Governing equations and discretization

2.1 Compressible MHD equations

The single fluid compressible adiabatic MHD equations describe the time evolution of the mass density ρ , the momentum $\rho \mathbf{v}$ (with velocity \mathbf{v}), the total energy density e and the magnetic field \mathbf{b} through:

$$\partial_t \rho = -\nabla \cdot (\rho \mathbf{v}), \quad (1)$$

$$\partial_t (\rho \mathbf{v}) = -\nabla \cdot \left(\rho \mathbf{v} \mathbf{v}^T + \left(p + \frac{1}{2} |\mathbf{b}|^2 \right) \mathbf{I} - \mathbf{b} \mathbf{b}^T - \underline{\boldsymbol{\sigma}} \right) + \mathbf{f}_K, \quad (2)$$

$$\partial_t e = -\nabla \cdot \left(\left(e + p + \frac{1}{2} |\mathbf{b}|^2 \right) \mathbf{v} - (\mathbf{v} \cdot \mathbf{b}) \mathbf{b} \right) - S_e + \mathbf{f}_{eKM}, \quad (3)$$

$$\partial_t \mathbf{b} = -\nabla \times (-\mathbf{v} \times \mathbf{b} + \eta \nabla \times \mathbf{b}) + \mathbf{f}_M, \quad (4)$$

$$\nabla \cdot \mathbf{b} = 0. \quad (5)$$

The 3×3 identity matrix is denoted by \mathbf{I} . The total energy density e is the sum of the kinetic, $\rho |\mathbf{v}|^2/2$, magnetic, $|\mathbf{b}|^2/2$ and internal, $p/(\gamma - 1)$, energy densities. Thus, the thermal pressure, p , is given by:

$$p = (\gamma - 1) \left(e - \frac{1}{2} \rho |\mathbf{v}|^2 - \frac{1}{2} |\mathbf{b}|^2 \right). \quad (6)$$

In driven turbulence, energy is injected by a kinetic \mathbf{f}_K and a magnetic \mathbf{f}_M forcing. These two forcing mechanisms also affect the total energy density through the \mathbf{f}_{eKM} term; these are described in section 3.5. A statistically stationary state is reached through the dynamical balance between the forcing terms and dissipation (both of numerical and physical nature). The physical dissipative terms are represented by the magnetic diffusivity η (caused by resistive effects), the internal energy sink modelled as Stefan-Boltzmann-like radiative losses:

$$S_e = \lambda U^4, \quad (7)$$

with $U = p/(\gamma - 1)$ and λ a constant, as well as the divergence of the linear viscous stress tensor:

$$\nabla \cdot \underline{\boldsymbol{\sigma}} = \mu \nabla^2 \mathbf{v} + \frac{1}{3} \mu \nabla (\nabla \cdot \mathbf{v}), \quad (8)$$

with μ the dynamic viscosity (the bulk viscosity is set to zero here).

In the isothermal case $\gamma \rightarrow 1$, eq. (3) does not need to be solved and the pressure is defined by $p = \rho c_s^2$ with c_s the constant sound-speed.

2.2 Finite-volume discretization

The hydrodynamic quantities $(\rho, \rho \mathbf{v})$ and the total energy density e are discretized as volume averages in a Cartesian coordinate system. The cubic domain $[0, L_x] \times [0, L_y] \times [0, L_z]$ consists of $N_x \times N_y \times N_z$ cells in the \mathbf{x} -, \mathbf{y} - and \mathbf{z} - directions with constant grid-sizes $\Delta x = L_x/N_x$, $\Delta y = L_y/N_y$ and $\Delta z = L_z/N_z$. The cells are centered at $x_i = (i + 1/2)\Delta x$, $y_j = (j + 1/2)\Delta y$, $z_k = (k + 1/2)\Delta z$. Their volume is $\Omega_{ijk} = [x_i - \Delta x/2, x_i + \Delta x/2] \times [y_j - \Delta y/2, y_j + \Delta y/2] \times [z_k - \Delta z/2, z_k + \Delta z/2]$.

As appropriate for finite-volume solvers, eqs. (1)-(3) are written in conservative form: $\partial_t q = -\nabla \cdot \mathbf{f}_q$. By the divergence theorem, the volume average of q over the cell Ω_{ijk} , denoted by \bar{q}_{ijk} , evolves in time as:

$$\begin{aligned} \partial_t \bar{q}_{ijk} &= \frac{1}{\Delta x \Delta y \Delta z} \iiint_{\Omega_{ijk}} \partial_t q dx dy dz, \\ &= -\frac{\bar{F}_{i+1/2,j,k}^q - \bar{F}_{i-1/2,j,k}^q}{\Delta x} - \frac{\bar{F}_{i,j+1/2,k}^q - \bar{F}_{i,j-1/2,k}^q}{\Delta y} - \frac{\bar{F}_{i,j,k+1/2}^q - \bar{F}_{i,j,k-1/2}^q}{\Delta z}, \end{aligned} \quad (9)$$

with $\bar{F}_n^q, n \in \{x, y, z\}$ representing the flux' area average on the cell face normal to the \mathbf{n} -direction. For example:

$$\bar{F}_{i\pm 1/2,j,k}^q = \frac{1}{\Delta y \Delta z} \iint_{S_{x,j,k}} \mathbf{f}_q(x_i \pm \Delta x/2, y, z) \cdot \mathbf{e}_x dy dz, \quad (10)$$

with $S_{x,j,k} = [y - \Delta y/2, y + \Delta y/2] \times [z - \Delta z/2, z + \Delta z/2]$ and \mathbf{e}_x the unit vector along the \mathbf{x} -direction. The averaged fluxes are defined in an analogous manner in the other directions. The explicit expressions for the fluxes, projected along \mathbf{e}_x , are derived from eqs. (1)-(3):

$$\begin{pmatrix} \mathbf{f}_\rho \cdot \mathbf{e}_x \\ \mathbf{f}_{\rho v_x} \cdot \mathbf{e}_x \\ \mathbf{f}_{\rho v_y} \cdot \mathbf{e}_x \\ \mathbf{f}_{\rho v_z} \cdot \mathbf{e}_x \\ \mathbf{f}_e \cdot \mathbf{e}_x \end{pmatrix} = \begin{pmatrix} \rho v_x^2 + p + |\mathbf{b}|^2/2 - b_x^2 - \mu(\partial_x v_x + \frac{1}{3}\nabla \cdot \mathbf{v}) \\ \rho v_x v_y - b_x b_y - \mu \partial_x v_y \\ \rho v_x v_z - b_x b_z - \mu \partial_x v_z \\ (e + p + |\mathbf{b}|^2/2)v_x - b_x(\mathbf{v} \cdot \mathbf{b}) \end{pmatrix}. \quad (11)$$

Appropriate circular permutations of the spatial dimensions ($x \rightarrow y \rightarrow z \rightarrow x$) give the projections along \mathbf{e}_y and \mathbf{e}_z .

The finite-volume approach guarantees that the physically conserved quantities (total mass, total impulse, total energy) are numerically conserved as well, up to machine precision. Indeed: everything that exits a cell through an interfacial flux enters a neighbouring one (e.g. $\bar{F}_{i+1/2,j,k}^q$ is a loss for cell Ω_{ijk} but a gain for cell $\Omega_{i+1,j,k}$).

2.3 Constrained-transport discretization

The constrained-transport approach discretizes the magnetic field such that its divergence (eq. (5)) is conserved up to machine precision [13]. Each magnetic field component is discretized as an area average on the faces normal to its respective direction. For cell Ω_{ijk} :

$$\bar{b}_{x,i-1/2,j,k} = \iint_{S_{x,j,k}} b_x(x_i - \Delta x/2, y, z) dy dz, \quad (12)$$

$$\bar{b}_{y,i,j-1/2,k} = \iint_{S_{y,k,i}} b_y(x, y_j - \Delta y/2, z) dz dx, \quad (13)$$

$$\bar{b}_{z,i,j,k-1/2} = \iint_{S_{z,i,j}} b_z(x, y, z_k - \Delta z/2) dx dy, \quad (14)$$

Applying Stoke's theorem on eq. (4) yields:

$$\partial_t \bar{b}_{x,i-1/2,j,k} = -\frac{\bar{E}_{z,i-1/2,j+1/2,k} - \bar{E}_{z,i-1/2,j-1/2,k}}{\Delta y} + \frac{\bar{E}_{y,i-1/2,j,k+1/2} - \bar{E}_{y,i-1/2,j,k-1/2}}{\Delta z}, \quad (15)$$

with $\mathbf{E} = -\mathbf{v} \times \mathbf{b} + \eta \nabla \times \mathbf{b}$ the electric field, the overbar meaning a line-average along its respective direction, for example:

$$\frac{z}{E}_{z,i-1/2,j+1/2,k} = \frac{1}{\Delta z} \int_{z_k-\Delta z/2}^{z_k+\Delta z/2} E_z(x_i - \Delta x/2, y_j + \Delta y/2, z) dz. \quad (16)$$

Similar relations apply for $\partial_t \bar{b}_y$ and $\partial_t \bar{b}_z$ with appropriate variable permutations. This staggered area-average definition of the magnetic field components leads to the conservation of a discretized formulation of $\nabla \cdot \mathbf{b}$ up to second-order approximation:

$$(\nabla \cdot \mathbf{b})_{i,j,k} \approx \frac{\bar{b}_{x,i+1/2,j,k} - \bar{b}_{x,i-1/2,j,k}}{\Delta x} + \frac{\bar{b}_{y,i,j+1/2,k} - \bar{b}_{y,i,j-1/2,k}}{\Delta y} + \frac{\bar{b}_{z,i,j,k+1/2} - \bar{b}_{z,i,j,k-1/2}}{\Delta z}, \quad (17)$$

since the terms of this approximation cancel pairwise [13, 14] (e.g. the circulation of \mathbf{E} on the edge $x = (i-1/2)\Delta x, y = (j-1/2)\Delta y, z \in [(k-1/2)\Delta z, (k+1/2)\Delta z]$ enters $\partial_t \bar{b}_{x,i-1/2,j,k}$ and $\partial_t \bar{b}_{y,i,j-1/2,k}$ with opposite signs). In this way, the constrained-transport approach is a counterpart to the finite-volume approach, where the flux exiting a cell cancels out with the one entering a neighbouring one. This implies that, if the divergence of \mathbf{b} is zero initially, it remains zero up to machine precision at all times.

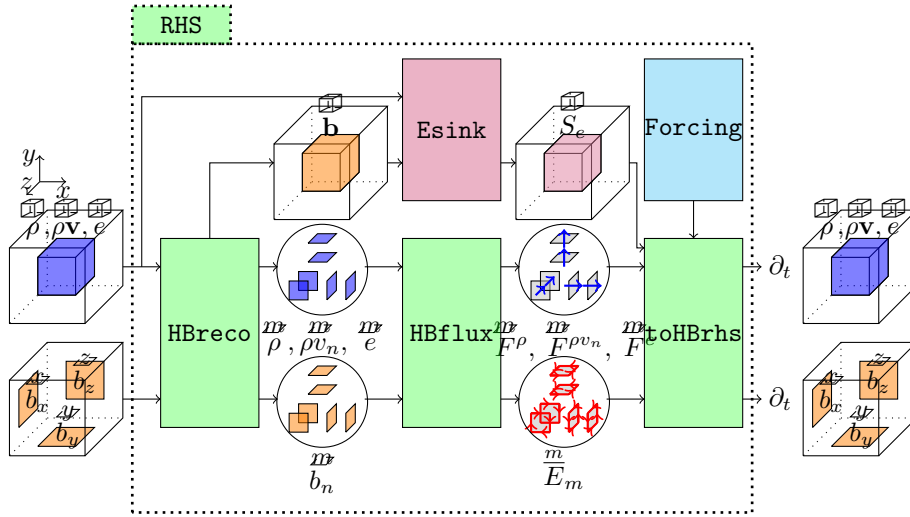


Figure 1: Right-hand-side computation's workflow.

3 Numerical solver

The fourth-order solver presented in [7] is extended up to tenth order of accuracy. The main structure of the right-hand side computation is shown in fig. 1: the solver reconstructs the fields at the interfaces between cells (**HBreco**, section 3.1), deduces the fluxes (**HBflux**, section 3.2) and from them the temporal derivatives (**toHBrhs**, section 3.3). The computation of the non-ideal terms: explicit viscous and resistive terms, alongside the internal energy sink, is described in section 3.4. The driving of the system is discussed in section 3.5. Finally, section 3.6 presents the time integrator and section 3.7 summarizes this method's keypoints.

3.1 Reconstruction module (**HBreco**)

This subsection describes the reconstruction module (**HBreco** in fig. 1), which is composed of two parts (fig. 2):

1. **Binterp**, which reconstructs volume averages of the magnetic field's components from the staggered constrained-transport discretization. This occurs through a polynomial interpolation. The magnetic field's volume averages are also needed to compute the internal energy sink (section 3.4.3).
2. **WENO**, which stands for Weighted Essentially Non-Oscillatory. It is a reconstruction procedure computing area averages of all quantities at the cell's interfaces from their volume average.

These two parts are described in the following.

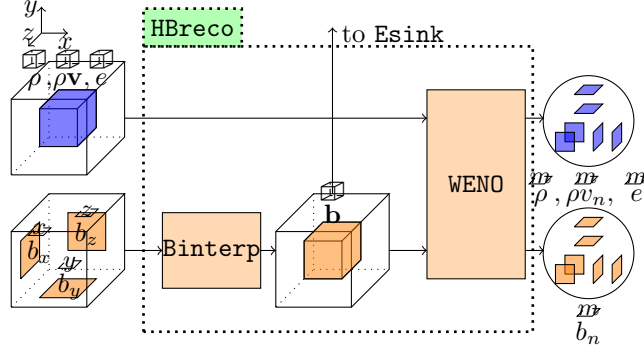


Figure 2: Reconstruction module.

3.1.1 Magnetic field interpolation (Binterp)

The constrained-transport approach evolves each magnetic field component b_n on the faces normal to its respective direction \mathbf{n} . However, \mathbf{b} needs to be known on all faces in order to compute, e.g., the fluxes (eq. (11)). A possibility is to first deduce volume averages, which are subsequently treated in the same way as the hydrodynamic quantities ($\rho, \rho \mathbf{v}$) and the total energy density e (see section 3.1.2).

The volume averages are computed as follows. For a given discretization order $m = 2q, q \in \mathbb{N}$, there is a unique polynomial P of degree at most $m - 1$ verifying:

$$P(x_l - \Delta x/2) = \overline{b}_{x,l-1/2,j,k}^{\mathcal{V}}, \forall l \in \{i - q + 1, \dots, i + q\}. \quad (18)$$

Its line-average along \mathbf{x} gives a m^{th} order approximation of the volume-averaged \overline{b}_x :

$$\frac{1}{\Delta x} \int_{x_i - \Delta x/2}^{x_i + \Delta x/2} P(x) dx = \frac{1}{\Delta x} \int_{x_i - \Delta x/2}^{x_i + \Delta x/2} \left(\overline{b}_x(x, y_j, z_k) + \mathcal{O}(\Delta x^m) \right) dx = \overline{b}_{x,i,j,k}^{\square} + \mathcal{O}(\Delta x^m). \quad (19)$$

All algebra done, this method yields:

$$\overline{b}_{x,i,j,k}^{\square} = \frac{1}{2} \left(\overline{b}_{x,j,k}^{\mathcal{V}(\frac{1}{2})} \right) + \mathcal{O}(\Delta x^2), \quad (20)$$

$$= \frac{1}{24} \left(13 \overline{b}_{x,j,k}^{\mathcal{V}(\frac{1}{2})} - \overline{b}_{x,j,k}^{\mathcal{V}(\frac{3}{2})} \right) + \mathcal{O}(\Delta x^4), \quad (21)$$

$$= \frac{1}{1440} \left(802 \overline{b}_{x,j,k}^{\mathcal{V}(\frac{1}{2})} - 93 \overline{b}_{x,j,k}^{\mathcal{V}(\frac{3}{2})} + 11 \overline{b}_{x,j,k}^{\mathcal{V}(\frac{5}{2})} \right) + \mathcal{O}(\Delta x^6), \quad (22)$$

$$= \frac{1}{120960} \left(68323 \overline{b}_{x,j,k}^{\mathcal{V}(\frac{1}{2})} - 9531 \overline{b}_{x,j,k}^{\mathcal{V}(\frac{3}{2})} + 1879 \overline{b}_{x,j,k}^{\mathcal{V}(\frac{5}{2})} - 191 \overline{b}_{x,j,k}^{\mathcal{V}(\frac{7}{2})} \right) + \mathcal{O}(\Delta x^8), \quad (23)$$

$$= \frac{1}{7257600} \left(4134338 \overline{b}_{x,j,k}^{\mathcal{V}(\frac{1}{2})} - 641776 \overline{b}_{x,j,k}^{\mathcal{V}(\frac{3}{2})} + 162680 \overline{b}_{x,j,k}^{\mathcal{V}(\frac{5}{2})} - 28939 \overline{b}_{x,j,k}^{\mathcal{V}(\frac{7}{2})} + 2497 \overline{b}_{x,j,k}^{\mathcal{V}(\frac{9}{2})} \right) + \mathcal{O}(\Delta x^{10}), \quad (24)$$

with $\overline{b}_{x,j,k}^{\mathcal{V}(p)} = \overline{b}_{x,i+p,j,k}^{\mathcal{V}} + \overline{b}_{x,i-p,j,k}^{\mathcal{V}}$. The extension to the \mathbf{y} - and \mathbf{z} -directions is straightforward.

Even though a non-oscillatory reconstruction would enhance the stability (cf. [15]), a polynomial interpolation is sufficient because each magnetic field component is continuous along its respective direction [16].

3.1.2 Weighted Essentially Non-Oscillatory reconstruction (WENO)

Weighted Essentially Non-Oscillatory (WENO) schemes allow high-order reconstruction in smooth regions while limiting oscillations in non-smooth ones. They are improvements of the Essentially Non-Oscillatory (ENO) schemes [17]. The first WENO scheme [18], third-order accurate, appeared in the 90s and has rapidly been extended to fifth-order [19]. A method to derive WENO schemes of arbitrarily high order of accuracy is provided in [20], and very high-order WENO schemes, with a discretization order up to 17 are given in [21, 22].

The main idea of a WENO reconstruction is to split the reconstruction stencil in substencils associated with different weights [20]. The weights are chosen so that, on the one hand, maximum accuracy is obtained in smooth regions, and, on the other hand, weights associated with non-smooth regions are vanishingly small. The method is presented here for a reconstruction in the \mathbf{x} -direction and can be straightforwardly transposed to the \mathbf{y} - and \mathbf{z} -directions. Given a stencil $\{x_{i-n}, x_{i-n+1}, \dots, x_i, \dots, x_{i+n}\}$ and a quantity q , there is a unique polynomial P^{opt} of degree at most $2n$ such that:

$$\frac{1}{\Delta x} \int_{x_{i+m-1/2}}^{x_{i+m+1/2}} P^{opt}(x) dx = \bar{q}_{i+m,j,k}, \forall m \in \{-n, \dots, n\}. \quad (25)$$

In smooth regions, this often-called “optimal polynomial” verifies:

$$P^{opt}(x) = \bar{q}^{\mathcal{AV}}(x, y_j, z_k) + \mathcal{O}(\Delta x^{2n+1}). \quad (26)$$

However, in regions containing strong gradients or even discontinuities, such as shock fronts, it would give an oscillatory reconstruction exhibiting over- and undershoots. To solve this issue, the $(2n+1)$ -long stencil is subdivided in the $n+1$ convex sub-stencils containing x_i : $\{x_{i-n}, \dots, x_i\}$, $\{x_{i-n+1}, \dots, x_i, x_{i+1}\}$, \dots , $\{x_i, \dots, x_{i+n}\}$. On each substencil, there is a unique optimal polynomial P^m of degree at most n which verifies eq. (25) for each cell in its substencil. At the cell boundaries, the aim is to write the “global” optimal polynomial P^{opt} as a linear combination of these “local” optimal polynomials P^m :

$$P^{opt}(x_i \pm \frac{\Delta x}{2}) = \sum_m d_m^\pm P^m(x_i \pm \frac{\Delta x}{2}), \quad (27)$$

with two sets of positive weights (d_m^\pm) , $\sum d_m^\pm = 1$.

Then, one designs other positive weights (w_m^\pm) with $\sum_m w_m^\pm = 1$ such that, on the one hand, $(w_m^\pm) \approx (d_m^\pm)$ in smooth regions, giving high-order accuracy, and, on the other hand, $w_m^\pm \rightarrow 0$ in substencils containing discontinuities. A design possibility is:

$$w_m^\pm = \frac{\alpha_m^\pm}{\sum_q \alpha_q^\pm}, \quad \alpha_m^\pm = \frac{d_m^\pm}{(\epsilon + IS_m)^p}, \quad (28)$$

with $\epsilon = 10^{-6}$, $p = 2$ as in [23, 7] and IS_m is a so-called “smoothness indicator”, defined as [19]:

$$IS_i^m = \sum_{l=1}^n \int_{x_i - \Delta x/2}^{x_i + \Delta x/2} (\Delta x)^{2l-1} (P_i^{m,(l)}(x))^2 dx, \quad (29)$$

with $P^{m,(l)}$ the l^{th} derivative of the P^m polynomial. The reconstructed values are finally:

$$\bar{q}^{\mathcal{AV}}(x_i \pm \Delta x/2, y_j, z_k) = \sum_m w_m^\pm P^m(x_i \pm \frac{\Delta x}{2}) + \epsilon_{reco}, \quad (30)$$

with ϵ_{reco} the discretization error, which goes as $\mathcal{O}(\Delta x^{2n+1})$ in smooth regions.

For the sake of brevity, we do not repeat here the numerical expressions for the smoothness indicators (IS^m), the weights (d_m^\pm) and the reconstructed values $\bar{q}_{i \pm 1/2, j, k}^{\mathcal{AV}}$ as a function of the volume averages $\bar{q}_{i,j,k}$, but refer to the literature [19, 21].

Remarks:

- A reconstruction of the magnetic field b_n component is not needed in the \mathbf{n} -direction: this area-average is already known in the constrained-transport framework.
- The procedure described here for volume-average \rightarrow area-average reconstruction is also used for area-average \rightarrow line-average reconstructions (section 3.2.3). The principle is the same, replacing the superscripts $\bar{\cdot}$ by $\bar{\cdot}^{\mathcal{AV}}$ and $\bar{\cdot}^{\mathcal{AV}}$ by $\bar{\cdot}^{\mathcal{AV}}$.

Although we consider only subsonic smooth flows in this work, we make use of so-called “global smoothness indicators” (GSI), both because of computing efficiency and in preparation of an extension to shocked problems. Indeed, as noted e.g. in [24, 7], the use of individual smoothness indicators, distinct for each reconstructed quantity, leads to significant oscillations in shocked regions, since the different reconstructed quantities experience one and the same shock in different ways. The GSI are computed as in [7]:

In order to obtain an order of accuracy strictly greater than two, our approach requires a passage through point values (**AtoP** and **PtoA**), described in section 3.2.2.

Finally, the non-ideal contributions through viscosity (**VISCO**) and magnetic diffusivity (**RESI**) are discussed in sections 3.4.1 and 3.4.2.

3.2.1 One-dimensional Riemann solver (1DRieS)

We employ the Rusanov approximation, also called “local Lax-Friedrichs” (LLF) [25, 26], which estimates the physical fluxes across an interface by assuming that all waves travel at the maximum propagation speed (the fast magneto-sonic speed). This rough approximation results in additional numerical dissipation, but is chosen here both for the sake of simplicity and to underline the benefits of higher-order discretizations. At the boundary $(i + 1/2, j, k)$, the LLF flux of field q is given by:

$$\mathbf{f}_{q,i+1/2,j,k}^{LLF} = \frac{1}{2}((\mathbf{f}_{q,i+1/2,j,k}^+ + \mathbf{f}_{q,i+1/2,j,k}^-) \cdot \mathbf{e}_x) - \frac{a_{i+1/2,j,k}^x}{2}(q_{i+1/2,j,k}^+ - q_{i+1/2,j,k}^-), \quad (33)$$

with the superscripts \pm denoting the states “right” and “left” of the interface: $x \rightarrow (x_i + \Delta x/2)^\pm$, reconstructed through the stencils centered at $(i + 1, j, k)$ and (i, j, k) respectively. The fluxes $\mathbf{f}_{q,i+1/2,j,k}^\pm$ (see eq. (11)) are obtained by plugging the quantities at the corresponding side of the interface. The treatment of the viscous term is described in section 3.4.1. The maximum speed of propagation of information, $a_{i+1/2,j,k}^x$, is estimated as:

$$a_{i+1/2,j,k}^x = \max((|\mathbf{v}_x| + c_f^x)^+, (|\mathbf{v}_x| + c_f^x)^-), \quad (34)$$

with c_f^x the fast magneto-sonic speed:

$$c_f^x = \sqrt{\frac{1}{2} \left(c_s^2 + c_A^2 + \sqrt{(c_s^2 + c_A^2)^2 - 4c_s^2 \frac{b_x^2}{\rho}} \right)}, \quad (35)$$

where $c_s = (\gamma p / \rho)^{1/2}$ and $c_A = (|\mathbf{b}|^2 / \rho)^{1/2}$ are the sound speed and the Alfvén speed, respectively. The formulas are analogous in the **y**- and **z**-directions.

The expressions above are strictly valid only for ideal MHD, i.e. for $\mu = \eta = 0$. In practice one can still use them in non-ideal MHD when the physical dissipation is small enough: $\max(\eta, \mu / \rho) / \min(\Delta x, \Delta y, \Delta z) \ll \min_{i \in \{x, y, z\}}(c_f^i)$ (see section 4.3). Nevertheless, when solving for the dissipative terms alone, the Riemann solver has to be changed in order to have a stable scheme, see section 4.2.

3.2.2 Passage through point values (AtoP and PtoA)

The reconstruction procedure (section 3.1.2) provides area-averages of arbitrarily high order of accuracy. However, one cannot plug them directly in the flux formulas (eq. (11)) without loss of numerical accuracy. Indeed, the fluxes consist of products and quotients of the fields $(\rho, \rho \mathbf{v}, e, \mathbf{b})$, e.g.:

$$\rho v_x v_y = (\rho v_x)(\rho v_y) / \rho. \quad (36)$$

This equality is not valid for area-averages:

$$\overline{(\rho v_x v_y)} \neq (\overline{\rho v_x})(\overline{\rho v_y}) / \overline{\rho}. \quad (37)$$

Identifying the area-averaged quantity with its point-value in the middle of the considered face gives a second-order error term [8, 9]. In the one-dimensional case, a Taylor expansion of \overline{q}_i , line-average of q over cell i , illustrates this:

$$\overline{q}_i = \frac{1}{\Delta x} \int_{-\Delta x/2}^{\Delta x/2} q(x_i + \epsilon) d\epsilon = \frac{1}{\Delta x} \int_{-\Delta x/2}^{\Delta x/2} (q(x_i) + \epsilon q'(x_i) + \mathcal{O}(\epsilon^2)) d\epsilon = q_i + \mathcal{O}(\Delta x^2). \quad (38)$$

A work-around is proposed in [8, 9]:

1. the reconstructed area-averages are transformed into point values at the desired order of accuracy (**AtoP** in fig. 3),
2. from them, the Riemann solver computes point-valued fluxes (**1DRieS**, section 3.2.1),
3. the point-valued fluxes are finally transformed into area-averaged fluxes (**PtoA**). They have the same order of accuracy as the point values obtained in step 1.

$j+4$					$\Sigma 40$				
$j+3$				$\Sigma 31$	$\Sigma 30$	$\Sigma 31$			
$j+2$			$\Sigma 22$	$\Sigma 21$	$\Sigma 20$	$\Sigma 21$	$\Sigma 22$		
$j+1$		$\Sigma 31$	$\Sigma 21$	$\Sigma 11$	$\Sigma 10$	$\Sigma 11$	$\Sigma 21$	$\Sigma 31$	
j	$\Sigma 40$	$\Sigma 30$	$\Sigma 20$	$\Sigma 10$	(i, j)	$\Sigma 10$	$\Sigma 20$	$\Sigma 30$	$\Sigma 40$
$j-1$		$\Sigma 31$	$\Sigma 21$	$\Sigma 11$	$\Sigma 10$	$\Sigma 11$	$\Sigma 21$	$\Sigma 31$	
$j-2$			$\Sigma 22$	$\Sigma 21$	$\Sigma 20$	$\Sigma 21$	$\Sigma 22$		
$j-3$				$\Sigma 31$	$\Sigma 30$	$\Sigma 31$			
$j-4$					$\Sigma 40$				
	$i-4$	$i-3$	$i-2$	$i-1$	i	$i+1$	$i+2$	$i+3$	$i+4$

Figure 4: Illustration of the different terms appearing in the area-averages \leftrightarrow point value transformations. A term with a superscript of the form Σmn with $m, n \in [0, 4]$ corresponds to the sum of the values in the cells where this superscript appears: it contains either four or eight terms.

The method described in appendix A produces the area-average \leftrightarrow point value transformations written below. The area-average \rightarrow point value transformation formulas are, up to tenth-order of accuracy:

$$q_{ij} = \tilde{\tilde{q}}_{ij} + \mathcal{O}(h^2), \quad (39)$$

$$q_{ij} = \frac{7}{6} \tilde{\tilde{q}}_{ij} - \frac{1}{24} \tilde{\tilde{q}}_{ij}^{\Sigma 10} + \mathcal{O}(h^4), \quad (40)$$

$$q_{ij} = \frac{1771}{1440} \tilde{\tilde{q}}_{ij} - \frac{23}{360} \tilde{\tilde{q}}_{ij}^{\Sigma 10} + \frac{3}{640} \tilde{\tilde{q}}_{ij}^{\Sigma 20} + \frac{1}{576} \tilde{\tilde{q}}_{ij}^{\Sigma 11} + \mathcal{O}(h^6), \quad (41)$$

$$q_{ij} = \frac{25451}{20160} \tilde{\tilde{q}}_{ij} - \frac{4973}{64512} \tilde{\tilde{q}}_{ij}^{\Sigma 10} + \frac{83}{8960} \tilde{\tilde{q}}_{ij}^{\Sigma 20} - \frac{5}{7168} \tilde{\tilde{q}}_{ij}^{\Sigma 30} + \frac{19}{5760} \tilde{\tilde{q}}_{ij}^{\Sigma 11} - \frac{1}{5120} \tilde{\tilde{q}}_{ij}^{\Sigma 21} + \mathcal{O}(h^8), \quad (42)$$

$$q_{ij} = \frac{5514407}{4300800} \tilde{\tilde{q}}_{ij} - \frac{69119}{806400} \tilde{\tilde{q}}_{ij}^{\Sigma 10} + \frac{42149}{3225600} \tilde{\tilde{q}}_{ij}^{\Sigma 20} - \frac{55}{32256} \tilde{\tilde{q}}_{ij}^{\Sigma 30} + \frac{35}{294912} \tilde{\tilde{q}}_{ij}^{\Sigma 40} + \frac{29173}{6451200} \tilde{\tilde{q}}_{ij}^{\Sigma 11} - \frac{41}{89600} \tilde{\tilde{q}}_{ij}^{\Sigma 21} + \frac{5}{172032} \tilde{\tilde{q}}_{ij}^{\Sigma 31} + \frac{9}{409600} \tilde{\tilde{q}}_{ij}^{\Sigma 22} + \mathcal{O}(h^{10}), \quad (43)$$

where $h = \Delta x + \Delta y$ and $\tilde{\tilde{q}}_{ij}^{\Sigma mn}$, $m \geq n \geq 0$ is the sum of all area-averages where one offset with respect to (i, j) is $\pm m$ and the other $\pm n$. Each possible combination of offsets $(\pm m, \pm n)$, $(\pm n, \pm m)$ is considered only once, thus, this sum contains eight terms, unless $n = 0$ or $m = n$, in which case it contains four terms (see fig. 4). Thus, for $m > 0$:

$$\tilde{\tilde{q}}_{ij}^{\Sigma mn} \underset{m>n>0}{=} \tilde{\tilde{q}}_{i+m,j+n} + \tilde{\tilde{q}}_{i+m,j-n} + \tilde{\tilde{q}}_{i-m,j+n} + \tilde{\tilde{q}}_{i-m,j-n} + \tilde{\tilde{q}}_{i+n,j+m} + \tilde{\tilde{q}}_{i+n,j-m} + \tilde{\tilde{q}}_{i-n,j+m} + \tilde{\tilde{q}}_{i-n,j-m} \quad (44)$$

$$\tilde{\tilde{q}}_{ij}^{\Sigma mm} = \tilde{\tilde{q}}_{i+m,j+m} + \tilde{\tilde{q}}_{i+m,j-m} + \tilde{\tilde{q}}_{i-m,j+m} + \tilde{\tilde{q}}_{i-m,j-m}, \quad (45)$$

$$\tilde{\tilde{q}}_{ij}^{\Sigma m0} = \tilde{\tilde{q}}_{i+m,j} + \tilde{\tilde{q}}_{i-m,j} + \tilde{\tilde{q}}_{i,j+m} + \tilde{\tilde{q}}_{i,j-m}. \quad (46)$$

Using the same notation for the point values: $q^{\Sigma mn}$, the point-to-area transformations needed for the transformation of the point-valued fluxes (PtoA block) are given by:

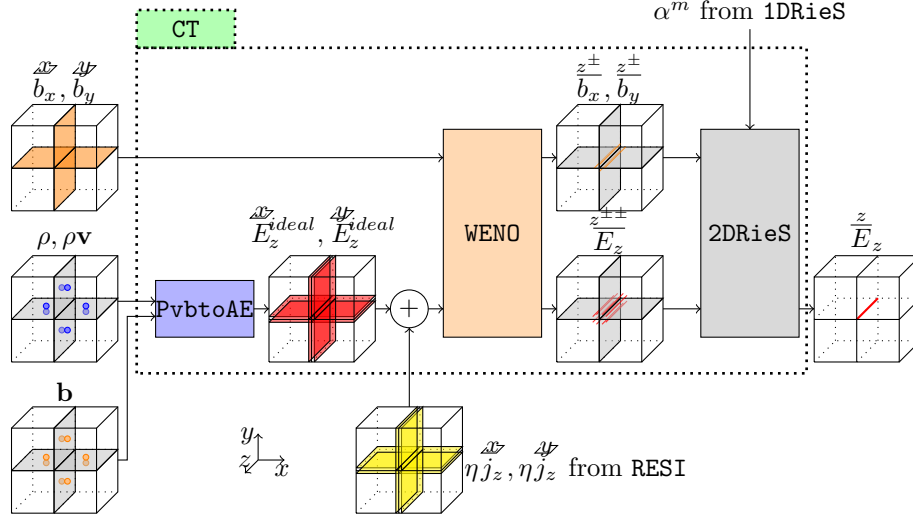


Figure 5: Constrained-transport module.

$$\tilde{q}_{ij} = q_{ij} + \mathcal{O}(h^2), \quad (47)$$

$$\tilde{q}_{ij} = \frac{5}{6}q_{ij} + \frac{1}{24}q_{ij}^{\Sigma_{10}} + \mathcal{O}(h^4), \quad (48)$$

$$\tilde{q}_{ij} = \frac{1159}{1440}q_{ij} + \frac{1}{20}q_{ij}^{\Sigma_{10}} - \frac{17}{5760}q_{ij}^{\Sigma_{20}} + \frac{1}{576}q_{ij}^{\Sigma_{11}} + \mathcal{O}(h^6), \quad (49)$$

$$\tilde{q}_{ij} = \frac{47939}{60480}q_{ij} + \frac{52223}{967680}q_{ij}^{\Sigma_{10}} - \frac{241}{48384}q_{ij}^{\Sigma_{20}} + \frac{367}{967680}q_{ij}^{\Sigma_{30}} + \frac{47}{17280}q_{ij}^{\Sigma_{11}} - \frac{17}{138240}q_{ij}^{\Sigma_{21}} + \mathcal{O}(h^8), \quad (50)$$

$$\begin{aligned} \tilde{q}_{ij} = & \frac{91251029}{116121600}q_{ij} + \frac{163519}{2903040}q_{ij}^{\Sigma_{10}} - \frac{186331}{29030400}q_{ij}^{\Sigma_{20}} + \frac{12011}{14515200}q_{ij}^{\Sigma_{30}} \\ & - \frac{27859}{464486400}q_{ij}^{\Sigma_{40}} + \frac{193537}{58060800}q_{ij}^{\Sigma_{11}} - \frac{3667}{14515200}q_{ij}^{\Sigma_{21}} + \frac{367}{23224320}q_{ij}^{\Sigma_{31}} + \frac{289}{33177600}q_{ij}^{\Sigma_{22}} + \mathcal{O}(h^{10}). \end{aligned} \quad (51)$$

The formulas above, for area-averages normal to \mathbf{z} , are generalizable for the other directions in a straightforward way.

From these area-averages \leftrightarrow point values transformations, one can deduce line-averages \leftrightarrow point values transformations, which are needed when solving two-dimensional problems, see appendix A.4. When applying an internal energy sink (section 3.4.3) or some driving to the system (section 3.5), one needs however volume-averages \leftrightarrow point values transformations. These formulas are given in appendix A.3.

3.2.3 Constrained-transport module (CT)

The key element in the CT module (fig. 5) is the two-dimensional Riemann solver (2DRieS), which computes the line-averaged electric field required to update the magnetic field components (eq. (15)). The method is presented here for the z component: \tilde{E}_z and is analogous for \tilde{E}_x and \tilde{E}_y with appropriate permutations. In this work, the line-averaged electric field is approximated by a multidimensional version of the LLF approximation [27], for the sake of simplicity. Improvements are available e.g. in [28]. At a certain edge of a numerical grid cell, e.g. $(i-1/2, j-1/2, k)$:

$$\tilde{E}_z = \frac{1}{4} \left[\overline{E}_z^{++} + \overline{E}_z^{+-} + \overline{E}_z^{-+} + \overline{E}_z^{--} \right] + \frac{S}{2} \left(\frac{z^+}{b_y} - \frac{z^-}{b_y} \right) - \frac{S}{2} \left(\frac{z^+}{b_x} - \frac{z^-}{b_x} \right), \quad (52)$$

where the positional subscripts are omitted in order to limit the amount of notation: all are at $(i-1/2, j-1/2, k)$. The first term is the average of four line-averaged electric field, with \overline{E}_z^{mn} , $m, n \in \{+, -\}$ meaning the value obtained through reconstructions at the position $x \rightarrow (x_i - \Delta x/2)^m$, $y \rightarrow (y_j - \Delta y/2)^n$. This reconstruction procedure is described below. It corresponds to the smooth part of the flux. The two other terms correspond to the propagation of discontinuities: S is the maximum speed of propagation of information, estimated as:

$$S = \max(a_{i-1/2, j, k}^x, a_{i-1/2, j-1, k}^x, a_{i, j-1/2, k}^y, a_{i-1, j-1/2, k}^y), \quad (53)$$

where a^x and a^y are given by eq. (34). This choice is made for the sake of efficiency [29], as these have already been computed in the **1DRieS** block. One should ideally consider the maximum speed among the four reconstructed states.

The magnetic field line-averages, \bar{b}_x^{\pm} and \bar{b}_y^{\pm} , are obtained through WENO reconstruction of the area-averages (section 3.1.2). These area-averages are the ones used in the constrained-transport discretization, so that they do not need the passage through the blocks **Binterp** and **WENO** in the **HBreco** module. A reconstruction along \mathbf{y} of \bar{b}_x^{\pm} gives \bar{b}_x^{\pm} , where \pm means $y \rightarrow (y_j - \Delta y/2)^{\pm}$. Similarly, a reconstruction along \mathbf{x} of \bar{b}_y^{\pm} gives \bar{b}_y^{\pm} , for $x \rightarrow (x_i - \Delta x/2)^{\pm}$.

The four line-averaged electric field in eq. (52) are obtained through the following steps (here described only for the z -component):

1. Compute point values of the ideal (i.e. magnetic diffusivity $\eta = 0$) electric field: $E^{ideal} = -\mathbf{v} \times \mathbf{b}$ from the point values of $\rho, \rho\mathbf{v}$ and \mathbf{b} obtained from the **AtoP** block of the **HBflux** module.
2. Use a point value→area-average transformation (section 3.2.2) to deduce eight area-averages of E_z^{ideal} (two for each face surrounding e.g. the $(i - 1/2, j - 1/2, k)$ edge, one on each side). This step and the previous one are included in the **PvbttoAE** block (fig. 5).
3. If needed ($\eta > 0$), add the non-ideal part (see section 3.4.2) to obtain eight area-averages of the total E_z .
4. Perform eight WENO reconstructions of the area-averaged E_z : along \mathbf{y} for the faces normal to \mathbf{x} and along \mathbf{x} for the faces normal to \mathbf{y} . This gives eight line-averaged values of \bar{E}_z : two for each cell adjacent to the considered edge.
5. Assuming that the discontinuities occur only at cell boundaries, the two reconstructed values in each cell (one from the volume-averages→area-averages reconstruction along \mathbf{x} followed by an area-average→line-average reconstruction along \mathbf{y} , and the other from volume-averages→area-averages along \mathbf{y} followed by area-average→line-average along \mathbf{x}) are merged into one by taking their mean. This gives one state per cell: \bar{E}_z^{++} from $\Omega_{i,j,k}$, \bar{E}_z^{+-} from $\Omega_{i,j-1,k}$, \bar{E}_z^{-+} from $\Omega_{i-1,j,k}$ and \bar{E}_z^{--} from $\Omega_{i-1,j-1,k}$. These four states are used in the two-dimensional Riemann solver **2DRieS**.

3.3 Deduction of the right-hand side (toHBrhs)

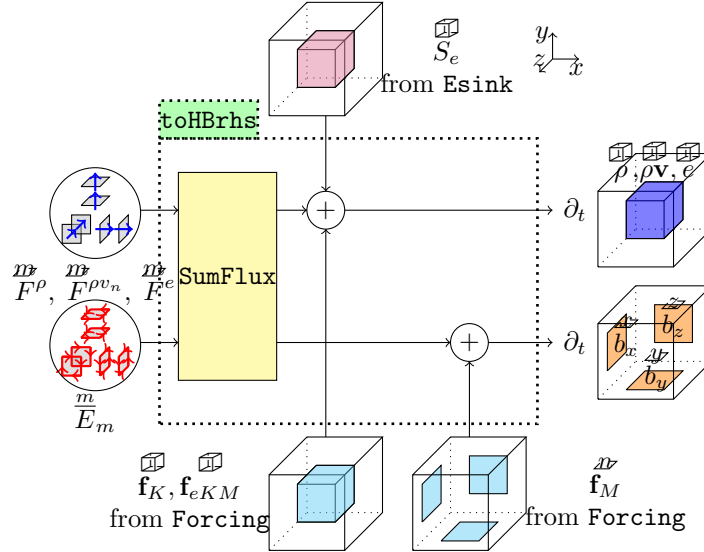


Figure 6: Deducing right-hand-side.

The right-hand side of the MHD equations (1)-(4) is determined by (see fig. 6, which is the block **toHBrhs** in fig. 1):

- plugging the interfacial fluxes (eq. (33), after passage through the **PtoA** block, fig. 3) into eq. (9),
- plugging the line-averaged electric fields (eq. (52)) into eq. (15). This step and the above one are represented by the **SumFlux** block in fig. 6,

- adding the internal energy sink term (see section 3.4.3),
- adding the forcing terms for the momentum, magnetic field and total energy density (see section 3.5).

3.4 Treatment of non-ideal terms

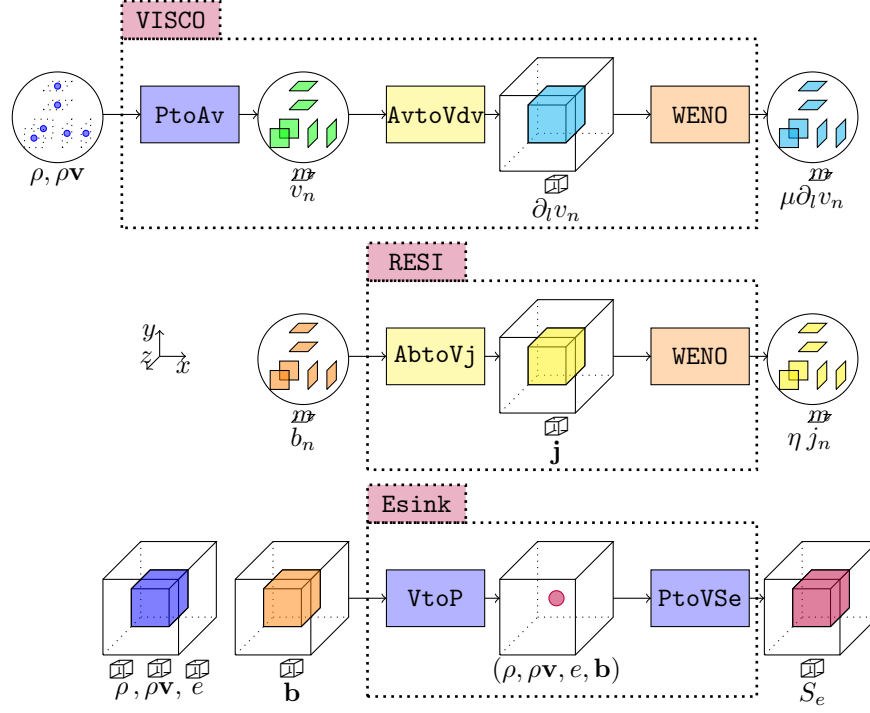


Figure 7: Modules for non-ideal terms.

The dissipative terms are computed as sketched in fig. 7. The next three subparts describe the treatment of the viscosity (VISCO), magnetic diffusivity (RESI) and internal energy sink (Esink), in this order.

3.4.1 Viscosity (VISCO)

The viscous contribution (eq. (8)) to the hydrodynamic fluxes is computed through the following steps:

1. From the point values in the middle of each interface between cells (after block **AtOP**, fig. 3): compute velocity field point values and deduce its area-averages through a point value→area-average transformation (section 3.2.2, block **PtoAv** in fig. 7).
2. Deduce volume averages of the derivatives $\partial_l v_n$ by noticing that:

$$(\partial_x v_n)_{i,j,k} = \frac{1}{\Delta x} \left(\frac{1}{\Delta y \Delta z} \iint dy dz \int \partial_x v_n dx \right) = \frac{\bar{v}_{n,i+1/2,j,k} - \bar{v}_{n,i-1/2,j,k}}{\Delta x}, \quad (54)$$

and similarly for the **y**- and **z**-directions (block **AvtoVdv** in fig. 7). Since eq. (54) is analytically exact, the scheme's discretization order is preserved.

3. Reconstruct area-averages of $\partial_l v_n$ through a WENO procedure (section 3.1.2). Four reconstructions are needed for the fluxes in each dimension: in dimension l , one needs $\partial_l v_n, n \in \{x, y, z\}$ and $\nabla \cdot \mathbf{v}$.
4. Multiply by the viscosity μ .
5. Since the LLF flux is used in this solver (section 3.2.1), it is enough for each interface to consider the average of the two reconstructed states surrounding it. This average is added to the computed area-averaged fluxes (see fig. 3). When using a different Riemann solver that does not have the same coefficients in front of the “left” and “right” states, one would need to plug these area-averages in the **AtOP** block (fig. 3) and provide them to the Riemann solver.

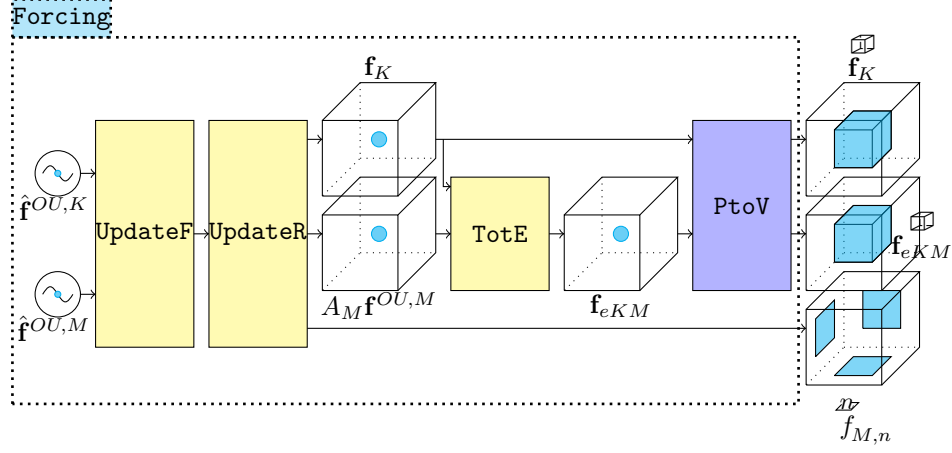


Figure 8: Forcing module.

3.4.2 Magnetic diffusivity (RESI)

The procedure for the magnetic diffusivity is very similar to that for the viscosity. The volume-averages of $\partial_l b_n$ with $l \neq n$ are computed from the area-averages (cf. eq. (54)), from which the volume averaged current $\mathbf{j} = \nabla \times \mathbf{b}$ is deduced (AbtoVj block, fig. 7), for example:

$$j_x = \frac{\overline{\overline{b}}_{z,i,j+1/2,k} - \overline{\overline{b}}_{z,i,j-1/2,k}}{\Delta y} - \frac{\overline{\overline{b}}_{y,i,j,k+1/2} - \overline{\overline{b}}_{y,i,j,k-1/2}}{\Delta z}. \quad (55)$$

After multiplication by η , a WENO procedure gives the area average of the electric field's non-ideal part. This term is added to the area-averaged electric field's ideal part (fig. 5).

3.4.3 Internal energy sink (Esink)

As pointed out in section 3.2.2, a passage through point values allows to build schemes of order strictly greater than two. Thus, the internal energy sink is computed through the following steps:

1. Transform the volume averages of $(\rho, \rho \mathbf{v}, e, \mathbf{b})$ to point values in the middle of the volume (VtoP in fig. 7).
2. Deduce the internal energy $U = p/(\gamma - 1)$ (cf. eq. (6)) and thus the Stefan-Boltzman like radiative loss term S_e (eq. (7)) as a point value.
3. Transform S_e to $\overline{\overline{S_e}}$ through a point value \rightarrow volume average transformation (PtoVSe).
4. Add this contribution to the right-hand side of e (cf. fig. 1).

The formulas for the point value \leftrightarrow volume average transformations are given in appendix A.3.

3.5 Forcing terms

Section 4.3 presents an example of application: a turbulent statistically stationary state. It results from a dynamical balance between large-scale energy injection and dissipative effects, both of physical and numerical nature. The mechanical and electromotive drivings (\mathbf{f}_K and \mathbf{f}_M in eqs. (2) and (4)) inject kinetic and magnetic energy at the largest scales, which is transported through nonlinear effects down to the smallest scales, where dissipative effects dominate. The \mathbf{f}_K and \mathbf{f}_M forcing terms affect the total energy equation through the term \mathbf{f}_{eKM} in eq. (3). These three terms are computed through the following steps (see fig. 8), explained in the next subsections:

- update the mechanical and electromotive drivings in Fourier space (block **UpdateF** in fig. 8, section 3.5.1),
- update and normalize them in real space to achieve a desired energy injection rate (block **UpdateR**, section 3.5.2),

- transform them to respect the chosen discretization: finite-volume using the constrained-transport approach (blocks TotE and PtoV, section 3.5.3).

Lastly, some remarks relevant in the context of turbulent MHD simulations are given in section 3.5.4.

3.5.1 Update in spectral space

Both kinetic and magnetic energies are injected through an Ornstein-Uhlenbeck process. The driving fields $\hat{\mathbf{f}}^{OU,K}$ (kinetic) and $\hat{\mathbf{f}}^{OU,M}$ (magnetic), set to zero initially, are both evolved in Fourier space according to the stochastic differential equation:

$$d\hat{\mathbf{f}}_{\mathbf{k}}^{OU,m}(t) = -\hat{\mathbf{f}}_{\mathbf{k}}^{OU,m}(t) \frac{dt}{t_{auto}} + F_0 \left(\frac{2\theta(\mathbf{k})^2}{t_{auto}} \right)^{1/2} \underline{\mathcal{P}}^\zeta \cdot d\mathbf{W}(t), \quad (56)$$

with t_{auto} the forcing autocorrelation time, F_0 an amplitude which value can be taken arbitrarily because of the normalization procedure described below and $\theta(\mathbf{k})$ a spectral profile explicated in section 4.3. A Wiener process $d\mathbf{W}(t) = dt\mathbf{N}(0, dt)$ modelizes a three-dimensional continuous random walk, with $\mathbf{N}(0, dt)$ a 3D Gaussian distribution with zero mean and standard deviation dt . The random numbers drawn are different for the kinetic and magnetic forcing, so that $\hat{\mathbf{f}}^{OU,M} \neq \hat{\mathbf{f}}^{OU,K}$. Purely solenoidal forcing fields are obtained by spectral projection $\mathcal{P}_{ij}^\zeta(\mathbf{k}) = \zeta\delta_{ij} + (1 - 2\zeta)\frac{k_i k_j}{|\mathbf{k}|^2}$ with $\zeta = 1$ and the three wavenumbers k_i of the corresponding wave vector.

3.5.2 Update and normalization in configuration space

The $\hat{\mathbf{f}}^{OU,K}$ and $\hat{\mathbf{f}}^{OU,M}$ complex fields are transformed to configuration space using a fast-Fourier transform algorithm, giving respectively $\mathbf{f}_{i,j,k}^{OU,K}$ and $\mathbf{f}_{i,j,k}^{OU,M}$, the values of the driving fields at the point (x_i, y_j, z_k) . The point-valued electromotive driving $\mathbf{f}_{i,j,k}^{OU,M}$ is not used to force the magnetic field (which is defined as staggered area-averages), but to update the total energy density e , see section 3.5.3. In order to get the area-averaged electromotive driving, the Fourier coefficients $\hat{\mathbf{f}}^{OU,M}$ are modified by (cf. eq. (12)):

$$\tilde{\mathbf{f}}_{x,\mathbf{k}}^{OU,M} = \hat{\mathbf{f}}_{x,\mathbf{k}}^{OU,M} \cdot \underbrace{e^{-ik_x \frac{\Delta x}{2}}}_{\text{Staggered field}} \cdot \overbrace{\frac{(e^{ik_y \frac{\Delta y}{2}} - e^{ik_y \frac{\Delta y}{2}})(e^{ik_z \frac{\Delta z}{2}} - e^{ik_z \frac{\Delta z}{2}})}{\Delta y \Delta z (ik_y)(ik_z)}}^{\text{Area average}}, \quad (57)$$

and similarly for the y - and z -components. After transformation to configuration space, the corresponding $\tilde{\mathcal{F}}_{x,i-1/2,j,k}^{OU,M}$, $\tilde{\mathcal{F}}_{y,i,j-1/2,k}^{OU,M}$ and $\tilde{\mathcal{F}}_{z,i,j,k-1/2}^{OU,M}$ can be applied to the staggered magnetic field without introducing non-solenoidal contributions.

In order to obtain prescribed constant kinetic and magnetic energy injection rates (ϵ_{inj}^K and ϵ_{inj}^M , respectively), the fields in configuration space are multiplied with two normalization factors A_K and A_M . These are taken as the largest root of the following second-order polynomial equations, which estimate in a first-order way the amount of energy injected during a time-interval Δt , if one would be using the Euler time integrator (cf. [30]):

$$\Delta \mathcal{E}_K = \frac{1}{2} A_K^2 \Delta t^2 \sum_{i,j,k} \overline{\rho}_{i,j,k} (\mathbf{f}_{i,j,k}^{OU,K})^2 + A_K \Delta t \sum_{i,j,k} (\overline{\rho \mathbf{v}})_{i,j,k} \cdot \mathbf{f}_{i,j,k}^{OU,K}, \quad (58)$$

$$\Delta \mathcal{E}_M = \frac{1}{2} A_M^2 \Delta t^2 \sum_{i,j,k} \mathbf{G}(f_{i,j,k}^{OU,M})^2 + A_M \Delta t \sum_{i,j,k} \mathbf{G}(b)_{i,j,k} \cdot \mathbf{G}(f_{i,j,k}^{OU,M}), \quad (59)$$

with $\mathbf{G}(g)_{i,j,k} = (\tilde{\mathcal{G}}_{x,i-1/2,j,k}, \tilde{\mathcal{G}}_{y,i,j-1/2,k}, \tilde{\mathcal{G}}_{z,i,j,k-1/2})$ the vector containing the 3 components of the staggered vector field \mathbf{g} , Δt the time-step used for the time integration (see section 3.6) and $\Delta \mathcal{E}_K = \epsilon_{inj}^K \Delta t$, $\Delta \mathcal{E}_M = \epsilon_{inj}^M \Delta t$.

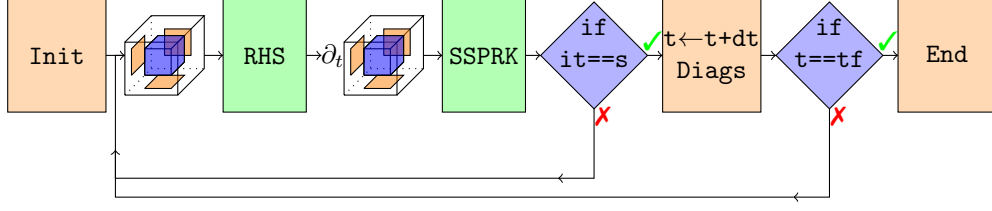


Figure 9: Complete structure of a solver. The current iteration of the s -stages SSPRK method is noted it . The variable timestep is dt . After initialization (module **Init**), a main loop occurs till the final time tf is reached when the code releases the memory and exits (module **End**).

3.5.3 Applying the forcing terms

While the staggered electromotive driving $\frac{\mathcal{A}r}{f}_{M,n} = A_M \frac{\mathcal{A}r}{f}_n^{OU,M}$ ($n \in \{x, y, z\}$) can be directly added to the right-hand side (see fig. 6), the mechanical driving is defined as a point-valued field at each (x_i, y_j, z_k) :

$$\mathbf{f}_{K,i,j,k} = \rho_{i,j,k} A_K \mathbf{f}_{i,j,k}^{OU,K}, \quad (60)$$

hence, a point value \rightarrow volume average transformation is performed before adding \mathbf{f}_K to the right-hand side of the momentum equation (block **PtoV** in fig. 8). Note the multiplication by the mass density ρ , explained in section 3.5.4.

Similarly, the effect of both mechanical and electromotive drivings on the energy equation eq. (3) is, at each point (x_i, y_j, z_k) :

$$\mathbf{f}_{eKM,i,j,k} = \mathbf{v}_{i,j,k} \cdot \mathbf{f}_{K,i,j,k} + \mathbf{b}_{i,j,k} \cdot (A_M \mathbf{f}_{i,j,k}^{OU,M}). \quad (61)$$

It is computed using the point-valued quantities from the block **AtoP** (fig. 3) and transformed into a volume-averaged quantity (block **TotE** followed by **PtoV** in fig. 8), so that \mathbf{f}_{eKM} is added to the right-hand side of e (fig. 6).

The formulas for point value \leftrightarrow volume averages transformations are given in appendix A.3.

3.5.4 Remarks for compressible MHD turbulent simulations

We conclude the description of the forcing module with two remarks relevant in the context of compressible MHD turbulence:

- The kinetic forcing occurs through an external acceleration field (i.e. it is of the form $\partial_t(\rho \mathbf{v}) = \rho \mathbf{f}$). This allows a broader inertial range in the turbulent spectra as compared to a forcing through an external *force* field (of the form $\partial_t(\rho \mathbf{v}) = \mathbf{g}$) [31, 32].
- The finite-volume approach guarantees the strict conservation of *momentum* up to machine precision. However, the statistical process that represents the turbulence driver can still generate a finite mean *velocity* component. The weak mean velocity field is thus removed at each call to the forcing procedure. This is important in the presence of magnetic fields as those break the Galilean invariance valid in purely hydrodynamic turbulence.

3.6 Time integration: Strong-Stability Preserving Runge-Kutta methods (SSPRK)

The computed right-hand side (RHS, sections 3.1-3.5) is plugged in a Strong Stability Preserving Runge-Kutta (SSPRK) time integrator (see the diagram for the whole solver, fig. 9). The SSPRK methods require several iterations, so that the RHS is computed s times (see the loop with the ending condition $it==s$ in fig. 9). After this, the simulation time t is updated. If needed, several diagnostics are written out, e.g. complete state of the system, or only its kinetic/magnetic energy, Fourier spectra, etc. Then, the time integration procedure is repeated. This is performed until the final time tf is reached.

SSPRK methods prevent additional oscillations resulting from inaccuracies in the time integration process [33, 34]. Although only smooth subsonic problems are considered in the present work, SSPRK methods also are very valuable in systems exhibiting discontinuities and shocks, e.g. turbulent supersonic fluids.

The second-order and fourth-order time integration methods are taken from [35] (pseudocode 1 with $s=10$ and pseudocode 3 of that reference, respectively). They are ten-stages single-step SSPRK methods. Ten-stages means that $s=10$

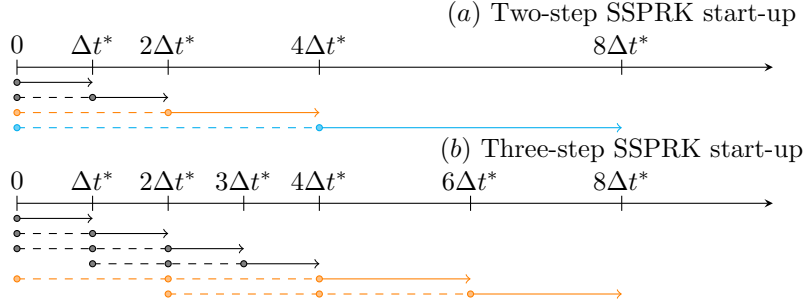


Figure 10: Start-up procedure for two- and three-step SSPRK methods, until $8\Delta t^*$ is reached. The dots linked with dashed lines correspond to the instants in time required to determine the next state. A change of color means a doubling of the time-step.

Method [source]	C_{CFL}	C_{VISCO}
$SSP(2, 10, 1)$ [35]	1.7	8
$SSP(4, 10, 1)$ [35]	1.8	1.4
$SSP(6, 10, 2)$ [40]	1.4	0.6
$SSP(8, 10, 3)$ [40]	1.2	0.3
$SSP(10, 20, 3)$ [40]	2.	0.5

Table 1: Time integrators and Courant number used for the simulations. Note that although the 10th order method has a higher C_{CFL} , it needs twenty stages as compared to the other ones that need only ten.

RHS computations are needed. Single-step means that the solution at the next instant $\mathbf{u}(\mathbf{x}, t + \Delta t)$ is computed solely from the solution at the instant t , $\mathbf{u}(\mathbf{x}, t)$.

However, for schemes of order strictly greater than four, no explicit single-step SSPRK method exists [36, 37]. For this reason, multi-step methods, which require the solution at several points in time, have been developed [38, 39, 40]. Two-step explicit methods, which require $\mathbf{u}(\mathbf{x}, t - \Delta t)$ in addition to $\mathbf{u}(\mathbf{x}, t)$ to compute $\mathbf{u}(\mathbf{x}, t + \Delta t)$, have order of accuracy at most eight [38]. Hence, for tenth order of accuracy, three-step methods (at least), which require $\mathbf{u}(\mathbf{x}, t - 2\Delta t)$ as well, are needed.

Consequently, the sixth-order method used is the two-step ten-stages one from [40]. The two-step eighth-order methods presented in [38] require a smaller time-step as compared to the three-step ten-stages one from [40], so that the latter is used. Finally, for tenth order of accuracy, a three-step twenty-stages method is used [40]. In the following, we denote the applied time integrators $SSP(p, s, n)$, with p the method's order of accuracy, s the number of stages and n the number of steps.

Since multi-step methods require several instants in time to determine the next one, a particular start-up procedure is needed. The start-up is performed by doubling step-by-step $\Delta t^* = \Delta t_{CFL}/2^\alpha$, $\alpha \in \mathbb{N}$, chosen initially small enough so that the overall accuracy of the scheme, p , is preserved [38]:

$$(\Delta t^*)^{q+1} = \mathcal{O}(\Delta t_{CFL}^p), \quad (62)$$

with q the order of the single-step procedure used for the first iteration. In this work, the first iteration is performed by the $SSP(q = 4, 10, 1)$ method. Then, for a two-step method $SSP(p, s, 2)$, $\mathbf{u}(0)$ and $\mathbf{u}(\Delta t^*)$ allow to deduce the solution at $2\Delta t^*$. Knowing $\mathbf{u}(0)$ and $\mathbf{u}(2\Delta t^*)$, the time-step can be doubled and one can determine $\mathbf{u}(4\Delta t^*)$, etc. (fig. 10.(a)). This process is repeated until Δt_{CFL} is reached. For a three-step method $SSP(p, s, 3)$, the $SSP(6, 10, 2)$ method is used to deduce $\mathbf{u}(2\Delta t^*)$ from $(\mathbf{u}(0), \mathbf{u}(\Delta t^*))$. Starting then, only the highest-order $SSP(p, s, 3)$ method is used. It is used two times before each doubling of the time-step: $\mathbf{u}(3\Delta t^*)$ and $\mathbf{u}(4\Delta t^*)$ are gained successively from $(\mathbf{u}(2\Delta t^*), \mathbf{u}(\Delta t^*), \mathbf{u}(0))$ and $(\mathbf{u}(3\Delta t^*), \mathbf{u}(2\Delta t^*), \mathbf{u}(\Delta t^*))$. The timestep can then be doubled: $(\mathbf{u}(4\Delta t^*), \mathbf{u}(2\Delta t^*), \mathbf{u}(0))$ allows to determine $\mathbf{u}(6\Delta t^*)$, etc. (fig. 10.(b)).

The time-step Δt is limited by the Courant-Friedrichs-Lewy criterion:

$$\Delta t \leq \Delta t_{CFL} = C_{CFL} \min_{i,j,k} (\Delta x/a_{i,j,k}^x, \Delta y/a_{i,j,k}^y, \Delta z/a_{i,j,k}^z), \quad (63)$$

with a^m the maximum speed of propagation of information in the \mathbf{m} -direction (see section 3.2.1) and C_{CFL} the Courant number.

In non-ideal systems, the time-step may be further reduced by the viscosity, the magnetic diffusivity or the internal energy sink:

$$\Delta t \leq \Delta t_{VISCO} = C_{VISCO} \frac{\min(\rho_{i,j,k}) \min(\Delta x, \Delta y, \Delta z)^2}{\mu}, \quad (64)$$

$$\Delta t \leq \Delta t_{RESI} = C_{RESI} \frac{\min(\Delta x, \Delta y, \Delta z)^2}{\eta}, \quad (65)$$

$$\Delta t \leq \Delta t_{Esink} = C_{Esink} \frac{1}{\lambda \max(U)^3}, \quad (66)$$

with a priori different constants $C_{VISCO}, C_{RESI}, C_{Esink}$. The numerical solver is stable for:

$$\Delta t \leq \min(\Delta t_{CFL}, \Delta t_{VISCO}, \Delta t_{RESI}, \Delta t_{Esink}). \quad (67)$$

The Courant numbers used in this work are listed in table 1.

3.7 Numerical method: summary

To summarize, the key points of the presented method are the following:

- The use of one-dimensional WENO reconstruction methods, which are computationally more affordable than multidimensional ones, especially with increasing order of accuracy.
- This is made possible by the transformation of area-averages into point values in the middle of each face up to arbitrarily high order of accuracy. The procedure prevents the need to compute several points on each face for the application of a quadrature rule.
- The viscous and resistive terms are formulated and computed in a way respecting the finite-volume and constrained-transport frameworks as well as the scheme's order.
- The internal energy sink and the forcing terms require point value \leftrightarrow volume average transformations, which can be derived to an arbitrarily high order of accuracy.
- High-order strong stability preserving explicit time integrators are available in the literature. For order strictly greater than four, these are multi-step methods.

4 Numerical tests

Numerical solvers of order 2, 4, 6, 8 and 10 are considered. They are denoted by S2, S4, S6, S8 and S10 and use the method of the corresponding order for the magnetic field volume interpolation (section 3.1.1), the passage through point values (sections 3.2.2 and 3.4.3) and the time integration (section 3.6). The employed WENO schemes (section 3.1.2) are of the next closest odd-order, that is 3, 5, 7, 9 and 11, respectively. The Courant numbers used are given in table 1.

The approach presented in this work is validated in two steps:

- first, a convergence test of the ideal MHD equations ($\mu = \eta = S_e = 0$) through the nonlinear 3D MHD vortex problem (section 4.1),
- second, a convergence test for the viscous and resistive terms (section 4.2).

Additionally, the MHD vortex test describes how a higher-order scheme leads to a higher computational efficiency by strongly reducing numerical non-ideal effects. This is also illustrated through the inertial range width and the level of visible structure details when simulating turbulent systems (section 4.3).

4.1 Validation of ideal MHD: 3D MHD vortex problem

The 3D MHD vortex is a nonlinear test case where a smooth magnetized vortex structure in force equilibrium is advected by a mean velocity field. The MHD vortex has first been introduced in 2D [41] and then extended to 3D [42] and has the initial conditions:

$$\begin{pmatrix} \rho \\ v_x \\ v_y \\ v_z \\ p \\ b_x \\ b_y \\ b_z \end{pmatrix} = \begin{pmatrix} 1 \\ 1 - y\kappa \exp\left[\phi(1 - r^2)\right] \\ 1 + x\kappa \exp\left[\phi(1 - r^2)\right] \\ 2 \\ p_0 + \frac{1}{4\phi} [\mu^2(1 - 2\phi(r^2 - z^2)) - \kappa^2\rho] \exp\left[2\phi(1 - r^2)\right] \\ -y\mu \exp\left[\phi(1 - r^2)\right] \\ x\mu \exp\left[\phi(1 - r^2)\right] \\ 0 \end{pmatrix}, \quad (68)$$

with $r = \sqrt{x^2 + y^2 + z^2}$ in the triply periodic computational domain $(x, y, z) \in [-5, 5] \times [-5, 5] \times [-5, 5]$ and the parameters $\kappa = \mu = 1/(2\pi)$, $\phi = 1.75$, $p_0 = 360$. The ambient pressure p_0 is set to be higher than in [41, 42], so that the advection speed is about one-tenth the speed of sound. The vortex is advected for one period of motion, until $t = 10$ and then compared to the initial conditions at $t = 0$. The error is measured as the average L1-distance between these two states in all $N_q = 8$ variables, $q \in \{\rho, \rho v_x, \rho v_y, \rho v_z, e, b_x, b_y, b_z\}$:

$$\delta Q(N) = \frac{1}{N_q N^3} \sum_q \sum_{i,j,k} |q(t=10) - q(t=0)|, \quad (69)$$

with $N = N_x = N_y = N_z$ the linear resolution in each dimension so that the system is discretized in N^3 grid-cells. The simulations are repeated at several resolutions $N \in \{64, 128, 256, 512\}$ and the experimental order of convergence *EOC*, expected to converge to the theoretical order of the solver for N high enough, is computed for $N \geq 128$ by:

$$EOC(N) = -\frac{\log(\delta Q(N)) - \log(\delta Q(N/2))}{\log(N) - \log(N/2)}. \quad (70)$$

In order to measure the impact of numerical dissipation, the proportion of lost energy is computed by:

$$E_{loss} = \frac{E(t=0) - E(t=10)}{E(t=0)}, \quad E = \sum_{i,j,k} \frac{1}{2} (\rho(\mathbf{v} - \mathbf{v}_{mean})^2 + \mathbf{b}^2)_{i,j,k}, \quad (71)$$

with \mathbf{v}_{mean} the mean velocity field, $(1, 1, 2)$, responsible for the advection, so that only the fluctuating field is considered.

Table 2 shows the measured errors, *EOC* and energy dissipation for the different resolutions. All the schemes S2, S4, S6, S8 and S10 exhibit an *EOC* consistent with their theoretical discretization order. At resolution 512^3 , the S10 scheme reaches an error level which lies in the region affected by the IEEE double precision representation of floating point numbers.

The dissipation is very large for the S2 scheme. This is because of the employed LLF Riemann solver. At low Mach numbers, the dissipative term $\propto a(q_R - q_L)$ (cf. eq. (33)), with $(q_R - q_L)$ the jump of q between the left and right states, does not scale correctly. For this solver, the dissipative term is dominated by the fast magneto-sonic speed, which leads to excessive dissipation [5]. When dealing with flows with a Mach number below 10^{-2} , commonly used approximate Riemann solvers, such as the Roe solver and HLL-type Riemann solvers, are indeed too dissipative to be of practical use when combined with second-order numerics [43]. With appropriate techniques these Riemann solvers can be modified to have a low dissipation over a wide range of Mach numbers (e.g. [5] for the Roe solver and [6] for the HLLD scheme). An alternative solution is to increase the discretization order, as in the present work. In that case, the jump $(q_R - q_L)$ becomes small enough to prevent excessive dissipation.

To illustrate the necessity of the passage through point values, a modification of the S6 solver is tested (S6P in table 2). For this solver, the passage through point values is suppressed. It converges as expected at a second-order rate (see eq. (38)). The reduced accuracy is however not reflected in the energy dissipation level (the E_{loss} values are very close to the S6 ones), hinting at dispersive effects. Similarly, using a second-order time integrator in place of the sixth-order one (scheme S6T, using a Courant number of 0.5 instead of 1.4) leads asymptotically to a convergence order of two.

Table 2 together with table 3 illustrate the gain in efficiency when seeking higher-order schemes for smooth problems. Even though these are more expensive than lower-order schemes at a given resolution (table 3), they allow to attain the

	Resolution	64^3	128^3	256^3	512^3
S2	δQ	7.7×10^{-4}	6.1×10^{-4}	2.6×10^{-4}	4.8×10^{-5}
	EOC	-	0.342	1.22	2.46
	E_{loss}	0.99	0.91	0.53	0.11
S4	δQ	3.7×10^{-4}	4.5×10^{-5}	1.9×10^{-6}	5.8×10^{-8}
	EOC	-	3.04	4.59	5.00
	E_{loss}	0.68	9.2×10^{-2}	3.4×10^{-3}	1.0×10^{-4}
S6	δQ	8.0×10^{-5}	1.1×10^{-6}	1.4×10^{-8}	1.8×10^{-10}
	EOC	-	6.25	6.23	6.31
	E_{loss}	0.12	1.8×10^{-3}	1.7×10^{-5}	1.4×10^{-7}
S8	δQ	6.6×10^{-5}	4.4×10^{-8}	1.4×10^{-10}	6.0×10^{-13}
	EOC	-	10.6	8.33	7.83
	E_{loss}	1.4×10^{-2}	5.0×10^{-5}	1.1×10^{-7}	2.0×10^{-10}
S10	δQ	1.5×10^{-4}	4.4×10^{-9}	2.9×10^{-12}	8.2×10^{-13}
	EOC	-	15.1	10.6	1.82
	E_{loss}	1.4×10^{-3}	1.3×10^{-6}	8.5×10^{-10}	2.2×10^{-13}
S6P	δQ	7.5×10^{-5}	1.5×10^{-6}	1.9×10^{-7}	4.7×10^{-8}
	EOC	-	5.68	2.93	2.03
	E_{loss}	0.12	1.8×10^{-3}	1.7×10^{-5}	1.5×10^{-7}
S6T	δQ	5.0×10^{-4}	1.1×10^{-6}	1.9×10^{-8}	3.0×10^{-9}
	EOC	-	8.89	5.79	2.68
	E_{loss}	0.12	1.8×10^{-3}	1.6×10^{-5}	1.4×10^{-7}

Table 2: 3D MHD vortex problem: measured error δQ after one period and corresponding experimental order of convergence EOC , as well as proportion of energy lost E_{loss} . The S6P and S6T schemes are modifications of the sixth-order S6 one, removing the passage through point values (S6P) or using a second-order time integrator (S6T) instead.

Solver	Average step duration (ASD)	Cost to reach a certain t_f
S2	1	1
S4	1.6	1.5
S6	2.2	2.7
S8	2.6	3.7
S10	7.6	6.5

Table 3: Computational cost for each solver: average step duration (ASD), as well as the cost to reach a certain instant (this corresponds to ASD divided by the Courant number, see table 1). The second-order scheme S2 is taken as the reference. The values are computed from the 512^3 runs, excluding the start-up procedure of the multi-step SSPRK methods (see section 3.6). The same number of cores, compiler options, processor types, etc. are used for all the runs.

same level of precision with regard to amplitude errors on substantially coarser grids. For example, the energy losses at resolution 512^3 for the S2 solver are comparable to those at resolution 128^3 for the S4 one. Even though the S4 solver is about 50% more expensive than the S2 one, a factor 4 in linear resolution N means a factor $4^4 = 256$ in computational costs (4^3 due to the increase in spatial resolution and an additional factor 4 because of the time-step reduction through the CFL criterion, see eq. (63)). Thus, when using S4 instead of S2, one can gain a factor of the order 100 in computational efficiency by performing a run of similar quality at a significantly lower resolution. The same pattern can be found for all increases of discretization order: comparing solvers S_n and $S(n+2)$, the energy dissipation of S_n at resolution 512^3 is close to the one of $S(n+2)$ at resolution 128^3 or 256^3 (or in between). The gain in computing time resulting from a lower resolution (a factor 16 to 256) is always higher than the loss because of the cost associated with using a higher-order scheme (a factor of order 2).

4.2 Validation of the dissipative terms

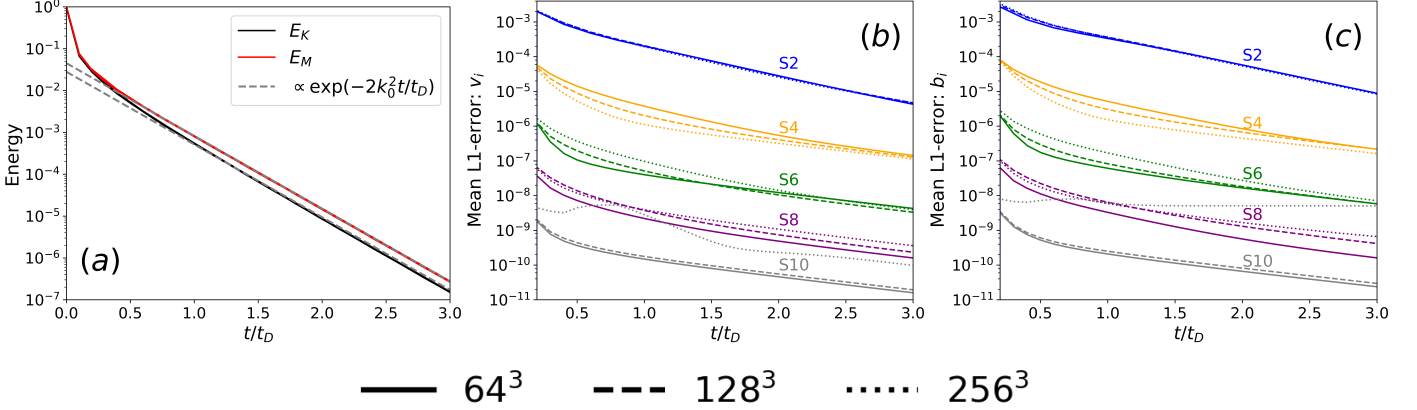


Figure 11: (a) Time evolution of total kinetic energy E_K and magnetic energy E_M (the smallest wavenumber present in the initial mixture of Fourier modes is $k_0 = \sqrt{2}$). (b) Time evolution of the L1-error of the velocity field. The curves at resolution $N^3 = 128^3$ (resp. 256^3) are multiplied by a factor 2^n (resp. 4^n) for the scheme S_n . (c) Time evolution of the L1-error of the magnetic field. The same rescaling as for the velocity field occurs for $N^3 = 128^3$ and 256^3 . The time is expressed in units of the characteristic diffusion time $t_D = 1/(\mu(2\pi/L)^2)$ with $L = 2\pi$ the domain size.

The viscous term's implementation is validated by considering the corresponding term in the momentum equation and assuming a constant $\rho = 1$:

$$\partial_t \mathbf{v} = \mu(\nabla^2 \mathbf{v} + \frac{1}{3} \nabla(\nabla \cdot \mathbf{v})). \quad (72)$$

This equation can be solved analytically through a passage in Fourier space:

$$\partial_t \begin{pmatrix} \hat{v}_{\mathbf{k},x} \\ \hat{v}_{\mathbf{k},y} \\ \hat{v}_{\mathbf{k},z} \end{pmatrix} = -\frac{\mu}{3} \underbrace{\begin{pmatrix} 3k^2 + k_x^2 & k_x k_y & k_x k_z \\ k_x k_y & 3k^2 + k_y^2 & k_y k_z \\ k_x k_z & k_y k_z & 3k^2 + k_z^2 \end{pmatrix}}_V \cdot \begin{pmatrix} \hat{v}_{\mathbf{k},x} \\ \hat{v}_{\mathbf{k},y} \\ \hat{v}_{\mathbf{k},z} \end{pmatrix}, \quad (73)$$

with $\hat{v}_{\mathbf{k},m}$ the Fourier coefficient of the velocity field's \mathbf{m} -component at the corresponding wavevector \mathbf{k} (and $k = |\mathbf{k}|$). The matrix V on the right-hand side is real symmetric, and hence diagonalizable:

$$V = PDP^{-1}, D = -\mu k^2 \begin{pmatrix} 1 & 0 & 0 \\ 0 & 1 & 0 \\ 0 & 0 & \frac{4}{3} \end{pmatrix}, P = \begin{pmatrix} -\frac{k_z}{k_x} & -\frac{k_y}{k_x} & \frac{k_x}{k_z} \\ 0 & 1 & \frac{k_y}{k_z} \\ 1 & 0 & 1 \end{pmatrix}, P^{-1} = \frac{1}{k^2} \begin{pmatrix} -k_x k_z & -k_y k_z & k_x^2 + k_y^2 \\ -k_x k_y & k_x^2 + k_z^2 & -k_y k_z \\ k_x k_z & k_y k_z & k_z^2 \end{pmatrix}. \quad (74)$$

The vector $\hat{\mathbf{w}}_{\mathbf{k}} = P^{-1} \hat{\mathbf{v}}_{\mathbf{k}}$ is governed by $\partial_t \hat{\mathbf{w}}_{\mathbf{k}} = D \hat{\mathbf{w}}_{\mathbf{k}}$, thus:

$$\hat{\mathbf{w}}_{\mathbf{k}}(t) = \begin{pmatrix} \hat{w}_{\mathbf{k},x}(0) \exp(-\mu k^2 t) \\ \hat{w}_{\mathbf{k},y}(0) \exp(-\mu k^2 t) \\ \hat{w}_{\mathbf{k},z}(0) \exp(-4\mu k^2 t/3) \end{pmatrix}. \quad (75)$$

From it, one deduces $\hat{\mathbf{v}}_{\mathbf{k}}(t) = P\hat{\mathbf{w}}_{\mathbf{k}}(t)$.

For the resistive term, the principle is the same, with the simpler equation:

$$\partial_t \mathbf{b} = \eta \nabla^2 \mathbf{b}, \quad (76)$$

whose solution in Fourier space is:

$$\hat{\mathbf{b}}_{\mathbf{k}}(t) = \hat{\mathbf{b}}_{\mathbf{k}}(0) \exp(-\eta k^2 t). \quad (77)$$

Thus, the viscous and resistive terms are tested by considering the time evolution of a linear superposition of $N_F = 30$ random Fourier modes for the velocity and magnetic fields in a triply periodic domain $[0, 2\pi]^3$. The modes (k_x, k_y, k_z) are drawn uniformly in the integer interval $[-5.5]^3$ and are used for both the velocity and magnetic fields in order to ease the comparison of their respective time evolution. For the velocity field, the Fourier coefficients of the three components $\hat{v}_{\mathbf{k},x}$, $\hat{v}_{\mathbf{k},y}$ and $\hat{v}_{\mathbf{k},z}$ receive a random amplitude and phase. For the magnetic field, the coefficients are chosen with random amplitude and phase but respecting two constraints: (i) they assure the magnetic field solenoidality (i.e. $k_x \hat{b}_{\mathbf{k},x} + k_y \hat{b}_{\mathbf{k},y} + k_z \hat{b}_{\mathbf{k},z} = 0$) and (ii) they contain the same amount of energy as the corresponding mode for the velocity field (i.e. $|\hat{b}_{\mathbf{k},x}|^2 + |\hat{b}_{\mathbf{k},y}|^2 + |\hat{b}_{\mathbf{k},z}|^2 = |\hat{v}_{\mathbf{k},x}|^2 + |\hat{v}_{\mathbf{k},y}|^2 + |\hat{v}_{\mathbf{k},z}|^2$), so as to ease comparison with the latter. When all the Fourier coefficients are determined, they are rescaled such that the total kinetic energy and total magnetic energy are initially equal to unity.

The equations (72) and (76) are solved in configuration space using the finite-volume and the constrained-transport approach respectively. For the WENO reconstruction step, a different smoothness indicator is computed for each variable individually (and not a global smoothness indicator, common for all variables, as presented in section 3.1.2). The timestep is limited according to the value of C_{VISCO} given in table 1. The viscosity and magnetic diffusivity are set to $\mu = \eta = 10^{-4}$. To measure the convergence of errors, the time evolutions given by the numerical schemes are compared to the analytical one at several resolutions.

The maximum speed of propagation used in the Riemann solver, a in eq. (33), is taken equal to the characteristic diffusion speed, e.g. in the \mathbf{x} -direction: $a^x = (4/3)\mu/\Delta x$. Similarly, for the 2D Riemann solver at a cell's edge along \mathbf{z} (see eq. (53)): $S = \eta/\min(\Delta x, \Delta y)$. Strictly speaking, the diffusive terms have a parabolic character: the characteristic manifold does not extend along the temporal dimension so that the information propagates at infinite speed. Nevertheless, the Laplacian kernel (Green's function) decreases very rapidly (exponentially with the square of the distance) so that a finite diffusion speed is a reasonable approximation. When the diffusive term is absent in the Riemann solver ($a = S = 0$), small-scale fluctuations resulting from numerical inaccuracies are amplified, leading to an unstable scheme.

Both the initialization of the fields and the comparison with the analytical solution require the transformation of the fields defined in Fourier space to configuration space. This has to be done in a way consistent with the chosen discretization. Assuming the coefficients $\hat{\mathbf{v}}_{\mathbf{k}}$ in Fourier space correspond to those at the collocation points (x_i, y_j, z_k) , the Fourier coefficients of the volume averages are given by:

$$\hat{\mathcal{V}}_{\mathbf{k}} = \hat{\mathbf{v}}_{\mathbf{k}} \cdot \frac{(e^{ik_x \frac{\Delta x}{2}} - e^{-ik_x \frac{\Delta x}{2}})(e^{ik_y \frac{\Delta y}{2}} - e^{-ik_y \frac{\Delta y}{2}})(e^{ik_z \frac{\Delta z}{2}} - e^{-ik_z \frac{\Delta z}{2}})}{\Delta x \Delta y \Delta z (ik_x)(ik_y)(ik_z)}. \quad (78)$$

Similarly, if $\hat{\mathbf{b}}_{\mathbf{k}}$ corresponds to the collocation points (x_i, y_j, z_k) , then

$$\hat{\mathcal{B}}_{x,\mathbf{k}} = \hat{b}_{x,\mathbf{k}} \cdot \frac{e^{-ik_x \frac{\Delta x}{2}}(e^{ik_y \frac{\Delta y}{2}} - e^{-ik_y \frac{\Delta y}{2}})(e^{ik_z \frac{\Delta z}{2}} - e^{-ik_z \frac{\Delta z}{2}})}{\Delta y \Delta z (ik_y)(ik_z)} \quad (79)$$

is the Fourier coefficient of the staggered area-averaged magnetic field along the \mathbf{x} -direction, and in an analogous manner for the \mathbf{y} - and \mathbf{z} -directions. This procedure is the same as the one needed to ensure that the electromotive forcing does not introduce non-solenoidal components to the magnetic field (cf. eq. (57)).

The results are shown in fig. 11. Subfigure (a) presents the time evolution of both the total kinetic energy E_K and magnetic energy E_M , for all the schemes and at all the resolutions. The shortest wavevector of the random mixture considered is $\mathbf{k}_0 = (1, 1, 0)$, with norm squared $k_0^2 = 2$. This is why the decay of both magnetic and kinetic energy goes asymptotically as $\exp(-2k_0^2 \mu t)$ (we have $\eta = \mu$). The decay is initially faster since the larger wavevectors start with an amount of energy comparable to that at \mathbf{k}_0 . Because of the $\nabla(\nabla \cdot \mathbf{v})$ term in eq. (72), the compressive part of the velocity field (along \mathbf{k} in Fourier space) decays faster, so that $E_K < E_M$.

The numerical time evolution follows very closely the exact one, even at the lowest accuracy (second-order scheme at resolution 64^3). Fig. 11.(b) and (c) show the time evolution of the error (as compared to the analytical exact solution) for the velocity and magnetic fields respectively. The mean of the L1-error in each component is considered. For the numerical scheme Sn , $n \in \{2, 4, 6, 8, 10\}$, the curve at resolution 128^3 is multiplied by a factor 2^n and the one at resolution 256^3 by a factor 4^n . Doing so leads to a collapse of the curves, confirming that the schemes converge at their expected

order. Similarly to the MHD vortex problem (section 4.1), the error is low enough for the S10 scheme to be impacted by the machine precision at resolution 256^3 (its curves are rescaled by a factor $4^{10} \approx 10^6$). The error in the magnetic field components stays constant at a level close to 8×10^{-15} , contrary to the one of the velocity field components, which decreases with time. This difference in behaviour between the magnetic and velocity fields is due to how floating-point arithmetics are done in a computing core. Such considerations are outside the scope of the present work.

4.3 Forced turbulence in a statistically stationary state

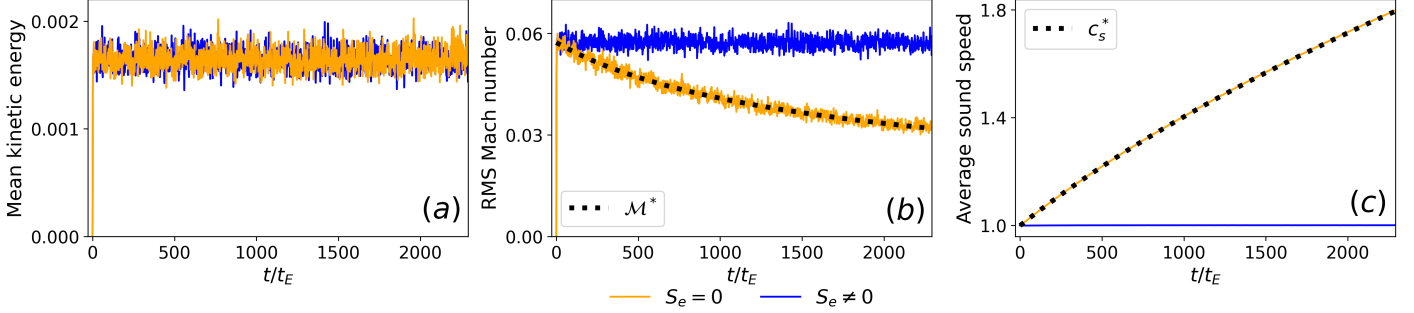


Figure 12: Time evolution of (a) the total kinetic energy, (b) the average sound speed and (c) the RMS Mach number. The dotted curves are theoretical predictions given in eqs. (82) and (83). The time is given in units of the large-eddy turnover time estimated as $t_E = L/(2\sqrt{2\mathcal{E}_{K,eq}/\rho_0})$ with $L = 1$.

As an example of application, a turbulent statistically stationary state is considered. It is obtained starting with a constant density monoatomic gas ($\rho = \rho_0 = 1$, $\gamma = 5/3$) at rest ($\mathbf{v} = 0$) in the triply periodic computational domain $[0, 1]^3$, at different resolutions. The total energy density, initially equal to the internal energy $U = p/(\gamma - 1)$, is chosen so that the initial sound speed $c_s = \sqrt{\gamma p/\rho_0}$ is constant and equal to 1.

The driving terms (section 3.5) inject kinetic and magnetic energies at large scales which cascade successively to smaller and smaller scales until dissipation (both of physical and numerical nature) dominates. The balance between the large scale injection and the dissipation leads to a turbulent statistically stationary state.

In the finite-volume framework, the kinetic and magnetic energies dissipated, either through the viscous and resistive terms or through numerical effects in the momentum and induction equations, are automatically transformed into heat. Indeed, the total energy density $\iiint e = \iiint (\frac{1}{2}\rho\mathbf{v}^2 + \frac{1}{2}\mathbf{b}^2 + U)$ is conserved down to machine precision, so that a loss of kinetic or magnetic energy means a raise in the internal energy U . Thus, one needs an internal energy sink S_e as well to reach a statistically stationary state.

The importance of the internal energy sink is illustrated in section 4.3.1. Sections 4.3.2 and 4.3.3 present turbulent data slices and Fourier spectra during the statistically stationary state which confirm that higher-order schemes allow to resolve finer structures at a given resolution.

4.3.1 Importance of the internal energy sink

Fig. 12 shows the time evolution of the total kinetic energy, the average sound speed and the root mean square (RMS) Mach number of two hydrodynamic runs executed with the S4 scheme at resolution 32^3 . One run is performed without internal energy sink S_e , and the other with an energy sink calibrated to keep the temperature constant. The physical viscosity is set to zero. The kinetic driving spectral profile (see eq. (56)) is taken as $\theta(\mathbf{k}) = 1$ for $1 \leq |\mathbf{k}| < 3$, zero otherwise and the energy injection rate is $\epsilon_{inj}^K = 10^{-4}$.

Because of numerical dissipation, the total kinetic energy stabilizes at a value fluctuating around $\mathcal{E}_{K,eq} = 1.64 \times 10^{-3}$ for both runs (fig. 12.(a)). However, the run without internal energy sink experiences an increase in temperature which translates into a decrease of the Mach number over time (fig. 12.(c)). The shape of the curve is expected. Indeed, the total energy in the system is governed by:

$$\mathcal{E}_T(t) = \iiint e(t) = U(t=0) + \epsilon_{inj}^K t. \quad (80)$$

Which gives an estimate of the mean pressure in the system, once the kinetic energy begins to fluctuate around its equilibrium value $\mathcal{E}_{K,eq}$:

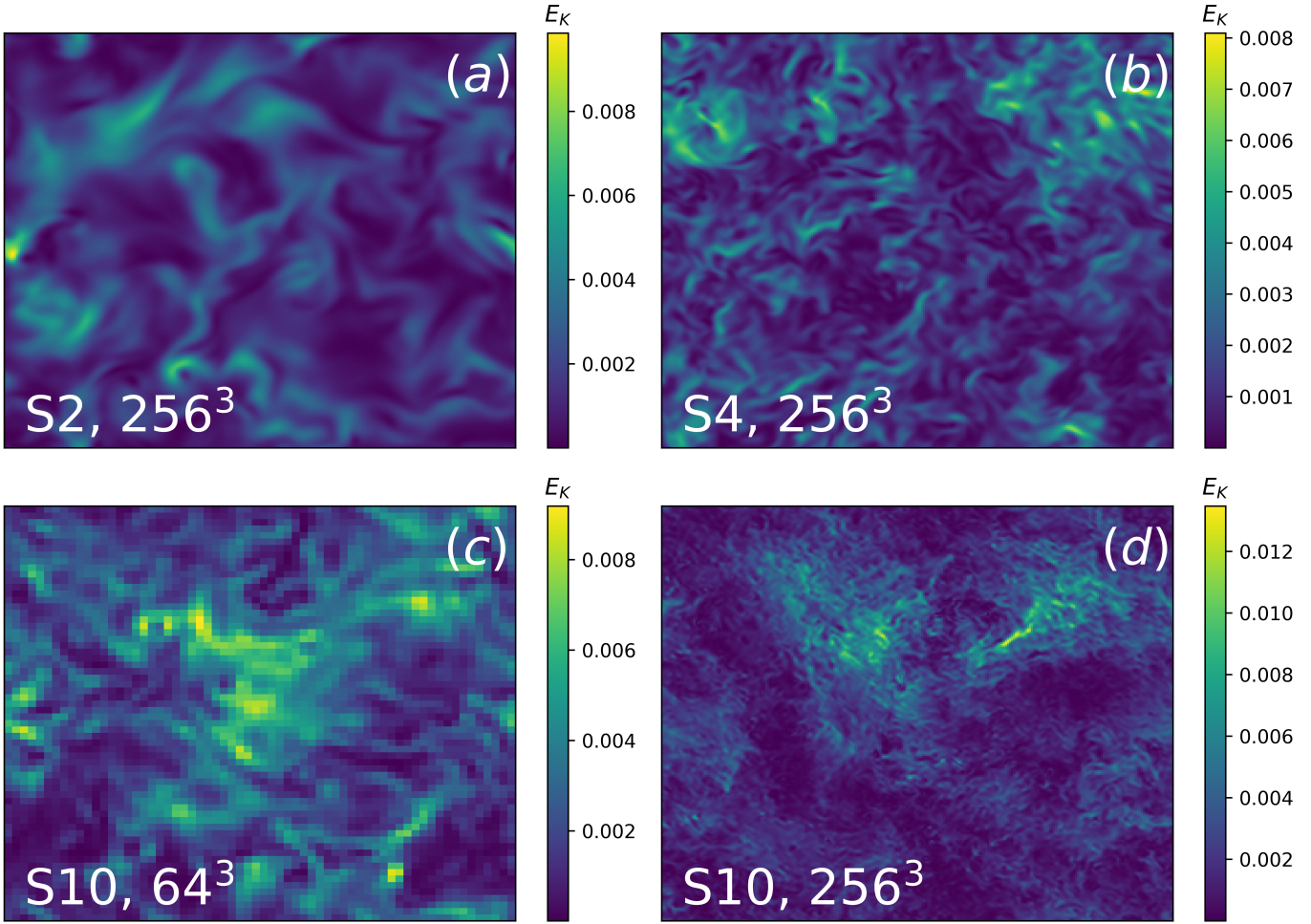


Figure 13: Slices of the kinetic energy during the hydrodynamic statistically stationary state.

$$p^*(t) = (\gamma - 1)(e - \mathcal{E}_{K,eq}) \approx (\gamma - 1)(U_0 + \epsilon_{inj}^K t - \mathcal{E}_{K,eq}). \quad (81)$$

At low Mach numbers, the mass density remains approximately constant $\rho \approx \rho_0$ so that one can estimate the mean sound speed as:

$$c_s^*(t) = \sqrt{\gamma p^*(t) / \rho_0}, \quad (82)$$

and hence the RMS Mach number should go as:

$$\mathcal{M}^*(t) = \sqrt{2\mathcal{E}_{K,eq} / \rho_0 / c_s^*(t)}. \quad (83)$$

The curves fig. 12.(b) and (c) follow these estimates very well.

In order to calibrate the internal energy sink $S_e = \lambda U^4$ so that the temperature stays constant (see fig. 12.(b)), one can estimate the internal energy variation through:

$$\partial_t U \approx \epsilon_{inj}^K - S_e, \quad (84)$$

which is zero for $\lambda = \epsilon_{inj}^K / U^4(t = 0)$.

4.3.2 Hydrodynamic statistically stationary state

In this section, the same hydrodynamic setting as in section 4.3.1 is considered, using the internal energy sink. The turbulent statistically stationary state obtained by schemes of different orders and at different resolutions are compared with one another.

Fig. 13 compares slices of the kinetic energy, obtained by the schemes S2, S4 and S10 at resolution 256^3 . The fourth-order scheme displays significantly finer structures as compared to the second-order one, but not nearly as fine as the tenth-order one. Fig. 13.(c) shows that the level of detail for the S10 scheme at the coarse 64^3 resolution is similar to the S2 scheme's one at the higher 256^3 resolution.

This visual impression is confirmed through the velocity power spectra (fig. 14). The extent of the inertial range, where the power spectrum goes as k^m with $m \approx -5/3$ consistent with Kolmogorov's phenomenology, is significantly broader for the fourth and tenth-order schemes. The inertial range for the S10 scheme at resolution 64^3 displays an extent between the one of the S2 and the one of the S4 schemes at resolution 256^3 .

This example of application illustrates that higher-order schemes can indeed be very beneficial when they allow to reach a certain results' accuracy at a significantly lower resolution as compared to, e.g., second-order schemes.

However, higher-order schemes may generate strong unphysical small scale fluctuations. This is illustrated in fig. 15, which displays significant bumps in the power spectra for the S6 and S8 schemes for the runs without viscosity, visible in configuration space as unphysical, i.e. essentially uncorrelated noise (fig. 15.(c)). These individually weak perturbations which distort the angle-averaged energy spectrum at small scales can efficiently be eliminated by adding a low level of physical viscosity ($\mu = 10^{-5}$, see subfigures (a), (b) and (c)). Please note that the generation of small scale-noise might be a general problem of the standard finite volume approach that has partially been masked by the larger numerical dissipation of common lower-order accurate numerical implementations.

4.3.3 MHD statistically stationary state

The MHD statistically stationary state is obtained using the same setting as in the hydrodynamic case, with the addition of an electromotive driving. It injects magnetic energy at the same rate as the mechanical forcing: $\epsilon_{inj}^M = \epsilon_{inj}^K = 10^{-4}$. The spectral profile (see eq. (56)) for the electromotive forcing is $\theta_B(\mathbf{k}) = 1$ for $4 \leq |\mathbf{k}| < 5$, and zero otherwise. The electromotive driving occurs at smaller spatial scales as compared to the mechanical driving so that enough modes are excited. If this is not the case, the lack of degrees of freedom can lead to an accumulation of cross-helicity (alignment between \mathbf{v} and \mathbf{b}) which affects the dynamics.

In order to maintain the temperature at its initial value, the factor of the internal energy sink is set to $\lambda = (\epsilon_{inj}^M + \epsilon_{inj}^K)/U^4(t=0)$ (cf. eq. (84), considering the magnetic energy injection as well).

As in the hydrodynamic case, a higher-order scheme reveals significantly finer structures at a given resolution (slices not shown). Contrary to the observations in the hydrodynamic case however, the generation of small-scale fluctuations for the S6 and S8 schemes is not as problematic in the MHD case, even in the absence of physical viscosity or magnetic diffusivity, see the power spectra in fig. 16. One may notice that even though the range with an approximate power-law scaling steadily grows with increasing order of accuracy, the growth is not as significant when moving from eighth to tenth order, as compared to the changes S2→S4, S4→S6 and S6→S8.

5 Conclusion

This work presents a computationally efficient method to implement high-order finite-volume compressible MHD solvers. The solvers use the constrained-transport approach to keep the magnetic field solenoidal. The key ingredient is a passage through point values, as proposed in [9, 8]: the area-averages computed by a dimension-by-dimension WENO algorithm are transformed to point values in the middle of the faces, which are used to compute point-valued interfacial fluxes, finally transformed back as area-averages. We supply the required explicit formulas up to tenth order of accuracy. This method requires only one reconstruction per face for any order of accuracy, contrary to other quadrature methods which may require an increasing number of values at each face with increasing order of accuracy.

The consistent inclusion of viscous and resistive terms respecting the finite-volume and constrained-transport formalism and preserving the order of accuracy has been shown. The usage of volume-average↔point value transformations allows to handle cooling functions and forcing terms in a high-order manner as well.

The numerical method is validated by several tests, including the advection of a 3D MHD vortex. The numerical dissipation decreases strongly when using higher-order numerics. Even though high-order schemes are more expensive at a given resolution (a factor of order 2 for an increase from order n to order $n+2$), the results' accuracy is comparable to that of lower order schemes at a significantly higher resolution (a factor 2 to 4 in linear resolution). This trend is also visible in the fine structures resolved by higher-order schemes in turbulent systems.

In conclusion, this work shows that extending existing codes to higher-order can be beneficial and reduce computing time for given accuracy requirements. For applications in smooth flows, using a higher-order scheme at a lower spatial resolution – as compared to the one needed for a second-order scheme to have a similar accuracy – can mean an overall gain in computing efficiency of a factor up to 10^3 . For applications in the case of non-smooth supersonic flows, common

in astrophysical contexts, the oscillating behaviour of higher-order polynomials near strong gradients leads to stability issues. A solution may be the use of some “flattening” (local reduction of the reconstruction order in the vicinity of strong gradients [7, 44, 45]), possibly associated with positivity preserving schemes [12].

Acknowledgments

The authors gratefully acknowledge G. Leidi for illuminating discussions, as well as the Max Planck Computing and Data Facility (MPCDF) for the computing resources.

Data Availability

The data that support the findings of this study are available from the corresponding author upon reasonable request.

Conflicts of interest

The authors declare that they have no known competing financial interests or personal relationships that could have appeared to influence the work reported in this paper.

Author Contributions

JMT: Writing - original draft, Conceptualization, Implementation and Numerical tests. WCM: Conceptualization, Writing-review and editing.

A Passage through point values

In this appendix, a general method to find volume-average \leftrightarrow point value transformation formulas which use point symmetric stencils around the considered cell is presented. This method has been sketched in [9, 8]. It is explicated in more details in sections A.1 and A.2. The obtained formulas are provided in sections A.3 and A.4.

A.1 Derivation of the formulas: an example

As an instructive example, this section presents the simpler cases of fourth-order and sixth-order line-average \leftrightarrow point value transformations. Writing \bar{q}_i the line-average of a quantity q over the cell $[x_i - \Delta x/2, x_i + \Delta x/2]$, a Taylor expansion up to sixth-order of accuracy gives (cf. eq. (38)):

$$\bar{q}_i = \int_{-\Delta x/2}^{\Delta x/2} q(x_i + \epsilon) d\epsilon = q_i + \frac{1}{24} \Delta x^2 \partial_x^2 q_i + \frac{1}{1920} \Delta x^4 \partial_x^4 q_i + \mathcal{O}(\Delta x^6), \quad (85)$$

with $q_i = q(x_i)$. In order to have a sixth-order approximation of q_i as a function of the known line-averages (that is, find a formula for a line-average \rightarrow point value transformation), one needs a way to eliminate the terms in $\partial_x^2 q_i$ and $\partial_x^4 q_i$. This can be achieved by considering $\bar{q}_i^{\Sigma\alpha} = \frac{x}{\bar{q}_i} \bar{q}_i^{\Sigma\alpha} = \frac{x}{\bar{q}_i} \bar{q}_i^{\Sigma\alpha}$, which gives, after expansion of the point-value derivatives $\partial_x^{2m} q_{i\pm\alpha}$ in Taylor series around x_i :

$$\begin{aligned} \bar{q}_i^{\Sigma\alpha} &= \left(2q_i + (\alpha\Delta x)^2 \partial_x^2 q_i + \frac{1}{12} (\alpha\Delta x)^4 \partial_x^4 q_i + \mathcal{O}(\Delta x^6) \right) + \frac{1}{24} \Delta x^2 \partial_x^2 \left(2q_i + (\alpha\Delta x)^2 \partial_x^2 q_i + \mathcal{O}(\Delta x^4) \right) \\ &+ \frac{1}{1920} \Delta x^4 \partial_x^4 \left(2q_i + \mathcal{O}(\Delta x^2) \right) + \mathcal{O}(\Delta x^6). \end{aligned} \quad (86)$$

Hence, for $\alpha \in \{1, 2\}$:

$$\bar{q}_i^{\Sigma 1} = 2q_i + \frac{13}{12} \Delta x^2 \partial_x^2 q_i + \frac{121}{960} \Delta x^4 \partial_x^4 q_i + \mathcal{O}(\Delta x^6), \quad (87)$$

$$\bar{q}_i^{\Sigma 2} = 2q_i + \frac{49}{12} \Delta x^2 \partial_x^2 q_i + \frac{1441}{960} \Delta x^4 \partial_x^4 q_i + \mathcal{O}(\Delta x^6). \quad (88)$$

One can find three constants A_0, A_1 and A_2 such that $A_0 \bar{q}_i^x + A_1 \bar{q}_i^{x\Sigma 1} + A_2 \bar{q}_i^{x\Sigma 2} = q_i + \mathcal{O}(\Delta x^6)$ by solving the system (see eqs. (85), (87) and (88)):

$$\begin{pmatrix} 1 & 2 & 2 \\ \frac{1}{24} & \frac{13}{12} & \frac{49}{12} \\ \frac{1}{1920} & \frac{13}{960} & \frac{1441}{960} \end{pmatrix} \begin{pmatrix} A_0 \\ A_1 \\ A_2 \end{pmatrix} = \begin{pmatrix} 1 \\ 0 \\ 0 \end{pmatrix}, \quad (89)$$

which has the solution $(\frac{1067}{960}, -\frac{29}{480}, \frac{3}{640})$ (cf. eq. 19 in [9]).

For a fourth-order line-average \rightarrow point value transformation, it is enough to remove the $\partial_x^2 q_i$ term. This can be done by using eqs. (85) and (87) to find B_0, B_1 such that $B_0 \bar{q}_i^x + B_1 \bar{q}_i^{x\Sigma 1} = q_i + \mathcal{O}(\Delta x^4)$. The linear system to solve consists of a submatrix of the previous one:

$$\begin{pmatrix} 1 & 2 \\ \frac{1}{24} & \frac{13}{12} \end{pmatrix} \begin{pmatrix} B_0 \\ B_1 \end{pmatrix} = \begin{pmatrix} 1 \\ 0 \end{pmatrix}, \quad (90)$$

which has the solution $(\frac{13}{12}, -\frac{1}{24})$ (cf. eq. 17 in [9]).

For point value \rightarrow line-average transformations, one can first rewrite the point values as a function of the line-averages only. Starting from eq. (85):

$$q_i = \bar{q}_i^x - A \Delta x^2 \partial_x^2 q_i - B \Delta x^4 \partial_x^4 q_i + \mathcal{O}(\Delta x^6), \quad (91)$$

with $A = \frac{1}{24}$ and $B = \frac{1}{1920}$, one can deduce recursively:

$$\begin{aligned} q_i &= \bar{q}_i^x - A \Delta x^2 \partial_x^2 (\bar{q}_i^x - A \Delta x^2 \partial_x^2 q_i + \mathcal{O}(\Delta x^4)) - B \Delta x^4 \partial_x^4 (\bar{q}_i^x + \mathcal{O}(\Delta x^2)) + \mathcal{O}(\Delta x^6), \\ &= \bar{q}_i^x - A \Delta x^2 \partial_x^2 \bar{q}_i^x + (A^2 - B) \Delta x^4 \partial_x^4 \bar{q}_i^x + \mathcal{O}(\Delta x^6), \\ &= \bar{q}_i^x - \frac{1}{24} \Delta x^2 \partial_x^2 \bar{q}_i^x + \frac{7}{5760} \Delta x^4 \partial_x^4 \bar{q}_i^x + \mathcal{O}(\Delta x^6). \end{aligned} \quad (92)$$

The principle is then the same as above: a Taylor expansion of $q_i^{\Sigma\alpha} = q_{i+\alpha} + q_{i-\alpha}$ in terms of \bar{q}_i^x , $\partial_x^2 \bar{q}_i^x$ and $\partial_x^4 \bar{q}_i^x$ for $\alpha \in \{1, 2\}$ gives three expressions. Combining them appropriately, one can find three constants C_0, C_1 and C_2 such that $C_0 q_i + C_1 q_i^{\Sigma 1} + C_2 q_i^{\Sigma 2} = \bar{q}_i^x + \mathcal{O}(\Delta x^6)$.

A.2 Derivation of the formulas: general case

For the general three-dimensional case, a Taylor expansion of the volume-average of q over the cell $\Omega_{ijk} = [x_i - \Delta x/2, x_i + \Delta x/2] \times [y_j - \Delta y/2, y_j + \Delta y/2] \times [z_k - \Delta z/2, z_k + \Delta z/2]$ gives:

$$\boxed{q}_{ijk} = \frac{1}{\Delta x \Delta y \Delta z} \sum_{n_x=0}^{\infty} \sum_{n_y=0}^{\infty} \sum_{n_z=0}^{\infty} \partial_x^{n_x} \partial_y^{n_y} \partial_z^{n_z} q_{ijk} \frac{1}{n_x! n_y! n_z!} \iiint_{\Omega_{ijk}} \epsilon_x^{n_x} \epsilon_y^{n_y} \epsilon_z^{n_z} d\epsilon_x d\epsilon_y d\epsilon_z. \quad (93)$$

The integral is non-zero only for even n_x, n_y, n_z . Thus, for $n_x = 2m_x, n_y = 2m_y, n_z = 2m_z$ with $m_x, m_y, m_z \in \mathbb{N}$:

$$\boxed{q}_{ijk} = \sum_{m_x=0}^{\infty} \sum_{m_y=0}^{\infty} \sum_{m_z=0}^{\infty} \frac{\Delta x^{2m_x} \Delta y^{2m_y} \Delta z^{2m_z} \partial_x^{2m_x} \partial_y^{2m_y} \partial_z^{2m_z} q_{ijk}}{(2m_x+1)!(2m_y+1)!(2m_z+1)! 2^{2(m_x+m_y+m_z)}}. \quad (94)$$

An expression up to an order of accuracy $2p$ contains thus all derivatives $\partial_x^{2m_x} \partial_y^{2m_y} \partial_z^{2m_z} q$ with $0 \leq 2(m_x + m_y + m_z) \leq 2(p-1)$. In order to eliminate these terms as in the example explicated in section A.1, one can consider a Taylor expansion

(in terms of derivatives of q) of all the terms $\boxed{q}_{ijk}^{\Sigma\alpha\beta\gamma}$, which consist of the sum of all volume-averages where one offset with respect to (i, j, k) is $\pm\alpha$, another $\pm\beta$ and the third one $\pm\gamma$, considering each combination of offset only once (generalizing the definition of $\bar{q}_{ij}^{\Sigma mn}$ to 3D, see section 3.2.2). A concrete expression for these terms is given in section A.3. With the offsets $\alpha, \beta, \gamma \geq 0$ and $0 \leq \alpha + \beta + \gamma \leq p-1$, there are as many such terms as there are different derivative terms up to order $2p$, and their Taylor expansion contain all the derivative terms that appear in eq. (94). Since the offsets considered are symmetric with respect to (i, j, k) , the odd derivative terms in the expansion cancel out.

In order to find a volume-average \rightarrow point value transformation formula of order $2p$, one can find coefficients $A_{\alpha\beta\gamma}$ such that:

$$\sum_{\alpha,\beta,\gamma} A_{\alpha\beta\gamma} \overline{q}_{ijk}^{\Sigma\alpha\beta\gamma} = q_{ijk} + \mathcal{O}(\Delta x^{2p} + \Delta y^{2p} + \Delta z^{2p}), \quad (95)$$

and hence solve a system of linear equations with as many equations as unknowns.

For the reverse transformation, from point values to volume averages, one can similarly to the 1D example of appendix A.1 rewrite eq. (94) as:

$$q_{ijk} = \overline{q}_{ijk} - \sum_{\substack{m_x, m_y, m_z=0 \\ m_x+m_y+m_z>0}}^{\infty} \frac{\Delta x^{2m_x} \Delta y^{2m_y} \Delta z^{2m_z} \partial_x^{2m_x} \partial_y^{2m_y} \partial_z^{2m_z} q_{ijk}}{(2m_x+1)!(2m_y+1)!(2m_z+1)!2^{2(m_x+m_y+m_z)}}. \quad (96)$$

And recursively (cf. eq. (92)) deduce an expression of the form:

$$q_{ijk} = \overline{q}_{ijk} - \sum_{\substack{m_x, m_y, m_z=0 \\ m_x+m_y+m_z>0}}^{m_x+m_y+m_z=p-1} K_{m_x, m_y, m_z} \partial_x^{2m_x} \partial_y^{2m_y} \partial_z^{2m_z} \overline{q}_{ijk} + \mathcal{O}(\Delta x^{2p} + \Delta y^{2p} + \Delta z^{2p}). \quad (97)$$

A Taylor expansion of the terms $\overline{q}_{ijk}^{\Sigma\alpha\beta\gamma}$ (in terms of derivatives of the volume-averages \overline{q}) gives then a linear system, whose solution delivers the coefficients for the point→volume-averages transformation.

A.3 Formulas for volume-averages↔point values transformations

Applying the method described above, one obtains the following formulas for volume-averages→point values transformations up to tenth order of accuracy:

$$q_{ijk} = \overline{q}_{ijk} + \mathcal{O}(h^2), \quad (98)$$

$$q_{ijk} = \frac{5}{4} \overline{q}_{ijk} - \frac{1}{24} \overline{q}_{ijk}^{\Sigma 100} + \mathcal{O}(h^4), \quad (99)$$

$$q_{ijk} = \frac{1301}{960} \overline{q}_{ijk} - \frac{97}{1440} \overline{q}_{ijk}^{\Sigma 100} + \frac{3}{640} \overline{q}_{ijk}^{\Sigma 200} + \frac{1}{576} \overline{q}_{ijk}^{\Sigma 110} + \mathcal{O}(h^6), \quad (100)$$

$$\begin{aligned} q_{ijk} = & \frac{341519}{241920} \overline{q}_{ijk} - \frac{80881}{967680} \overline{q}_{ijk}^{\Sigma 100} + \frac{173}{17920} \overline{q}_{ijk}^{\Sigma 200} - \frac{5}{7168} \overline{q}_{ijk}^{\Sigma 300} \\ & + \frac{119}{34560} \overline{q}_{ijk}^{\Sigma 110} - \frac{1}{5120} \overline{q}_{ijk}^{\Sigma 210} - \frac{1}{13824} \overline{q}_{ijk}^{\Sigma 111} + \mathcal{O}(h^8), \end{aligned} \quad (101)$$

$$\begin{aligned} q_{ijk} = & \frac{15997789}{11059200} \overline{q}_{ijk} - \frac{1829207}{19353600} \overline{q}_{ijk}^{\Sigma 100} + \frac{25751}{1843200} \overline{q}_{ijk}^{\Sigma 200} - \frac{65}{36864} \overline{q}_{ijk}^{\Sigma 300} \\ & + \frac{35}{294912} \overline{q}_{ijk}^{\Sigma 400} + \frac{11723}{2419200} \overline{q}_{ijk}^{\Sigma 110} - \frac{1019}{2150400} \overline{q}_{ijk}^{\Sigma 210} + \frac{5}{172032} \overline{q}_{ijk}^{\Sigma 310} \\ & + \frac{9}{409600} \overline{q}_{ijk}^{\Sigma 220} - \frac{47}{276480} \overline{q}_{ijk}^{\Sigma 111} + \frac{1}{122880} \overline{q}_{ijk}^{\Sigma 211} + \mathcal{O}(h^{10}), \end{aligned} \quad (102)$$

with $h = \Delta x + \Delta y + \Delta z$. The notation $\overline{q}_{ijk}^{\Sigma\alpha\beta\gamma}$ is explained in section A.2. Up to tenth-order of accuracy, one has either $\gamma = \beta$ or $\gamma = 0$, resulting in:

$$\begin{aligned}
\boxed{q}_{ijk}^{\Sigma\alpha\beta\beta} &= \boxed{q}_{i+\alpha,j+\beta,k+\beta} + \boxed{q}_{i+\alpha,j+\beta,k-\beta} + \boxed{q}_{i+\alpha,j-\beta,k+\beta} + \boxed{q}_{i+\alpha,j-\beta,k-\beta} \\
&+ \boxed{q}_{i-\alpha,j+\beta,k+\beta} + \boxed{q}_{i-\alpha,j+\beta,k-\beta} + \boxed{q}_{i-\alpha,j-\beta,k+\beta} + \boxed{q}_{i-\alpha,j-\beta,k-\beta} \\
&+ \boxed{q}_{i+\beta,j+\alpha,k+\beta} + \boxed{q}_{i+\beta,j+\alpha,k-\beta} + \boxed{q}_{i+\beta,j-\alpha,k+\beta} + \boxed{q}_{i+\beta,j-\alpha,k-\beta} \\
&+ \boxed{q}_{i-\beta,j+\alpha,k+\beta} + \boxed{q}_{i-\beta,j+\alpha,k-\beta} + \boxed{q}_{i-\beta,j-\alpha,k+\beta} + \boxed{q}_{i-\beta,j-\alpha,k-\beta} \\
&+ \boxed{q}_{i+\beta,j+\beta,k+\alpha} + \boxed{q}_{i+\beta,j+\beta,k-\alpha} + \boxed{q}_{i+\beta,j-\beta,k+\alpha} + \boxed{q}_{i+\beta,j-\beta,k-\alpha} \\
&+ \boxed{q}_{i-\beta,j+\beta,k+\alpha} + \boxed{q}_{i-\beta,j+\beta,k-\alpha} + \boxed{q}_{i-\beta,j-\beta,k+\alpha} + \boxed{q}_{i-\beta,j-\beta,k-\alpha}, \tag{103}
\end{aligned}$$

$$\begin{aligned}
\boxed{q}_{ijk}^{\Sigma\beta\beta\beta} &= \boxed{q}_{i+\beta,j+\beta,k+\beta} + \boxed{q}_{i+\beta,j+\beta,k-\beta} + \boxed{q}_{i+\beta,j-\beta,k+\beta} + \boxed{q}_{i+\beta,j-\beta,k-\beta} \\
&+ \boxed{q}_{i-\beta,j+\beta,k+\beta} + \boxed{q}_{i-\beta,j+\beta,k-\beta} + \boxed{q}_{i-\beta,j-\beta,k+\beta} + \boxed{q}_{i-\beta,j-\beta,k-\beta}, \tag{104}
\end{aligned}$$

$$\begin{aligned}
\boxed{q}_{ijk}^{\Sigma\alpha\beta 0} &= \boxed{q}_{i+\alpha,j+\beta,k} + \boxed{q}_{i+\alpha,j-\beta,k} + \boxed{q}_{i-\alpha,j+\beta,k} + \boxed{q}_{i-\alpha,j-\beta,k} \\
&+ \boxed{q}_{i+\beta,j+\alpha,k} + \boxed{q}_{i+\beta,j-\alpha,k} + \boxed{q}_{i-\beta,j+\alpha,k} + \boxed{q}_{i-\beta,j-\alpha,k} \\
&+ \boxed{q}_{i+\alpha,j,k+\beta} + \boxed{q}_{i+\alpha,j,k-\beta} + \boxed{q}_{i-\alpha,j,k+\beta} + \boxed{q}_{i-\alpha,j,k-\beta} \\
&+ \boxed{q}_{i+\beta,j,k+\alpha} + \boxed{q}_{i+\beta,j,k-\alpha} + \boxed{q}_{i-\beta,j,k+\alpha} + \boxed{q}_{i-\beta,j,k-\alpha} \\
&+ \boxed{q}_{i,j+\alpha,k+\beta} + \boxed{q}_{i,j+\alpha,k-\beta} + \boxed{q}_{i,j-\alpha,k+\beta} + \boxed{q}_{i,j-\alpha,k-\beta} \\
&+ \boxed{q}_{i,j+\beta,k+\alpha} + \boxed{q}_{i,j+\beta,k-\alpha} + \boxed{q}_{i,j-\beta,k+\alpha} + \boxed{q}_{i,j-\beta,k-\alpha}, \tag{105}
\end{aligned}$$

$$\begin{aligned}
\boxed{q}_{ijk}^{\Sigma\beta\beta 0} &= \boxed{q}_{i+\beta,j+\beta,k} + \boxed{q}_{i+\beta,j-\beta,k} + \boxed{q}_{i-\beta,j+\beta,k} + \boxed{q}_{i-\beta,j-\beta,k} \\
&+ \boxed{q}_{i+\beta,j,k+\beta} + \boxed{q}_{i+\beta,j,k-\beta} + \boxed{q}_{i-\beta,j,k+\beta} + \boxed{q}_{i-\beta,j,k-\beta} \\
&+ \boxed{q}_{i,j+\beta,k+\beta} + \boxed{q}_{i,j+\beta,k-\beta} + \boxed{q}_{i,j-\beta,k+\beta} + \boxed{q}_{i,j-\beta,k-\beta}, \tag{106}
\end{aligned}$$

$$\boxed{q}_{ijk}^{\Sigma\beta 0 0} = \boxed{q}_{i+\beta,j,k} + \boxed{q}_{i-\beta,j,k} + \boxed{q}_{i,j+\beta,k} + \boxed{q}_{i,j-\beta,k} + \boxed{q}_{i,j,k+\beta} + \boxed{q}_{i,j,k-\beta}. \tag{107}$$

Using the same notation for the sum of point-averages $q_{ijk}^{\Sigma\alpha\beta\gamma}$ with offsets $\pm\alpha, \pm\beta$ and $\pm\gamma$, the reverse point values \rightarrow volume-averages transformations are:

$$\boxed{q}_{ijk} = q_{ijk} + \mathcal{O}(h^2), \quad (108)$$

$$\boxed{q}_{ijk} = \frac{3}{4}q_{ijk} + \frac{1}{24}q_{ijk}^{\Sigma 100} + \mathcal{O}(h^4), \quad (109)$$

$$\boxed{q}_{ijk} = \frac{689}{960}q_{ijk} + \frac{67}{1440}q_{ijk}^{\Sigma 100} - \frac{17}{5760}q_{ijk}^{\Sigma 200} + \frac{1}{576}q_{ijk}^{\Sigma 110} + \mathcal{O}(h^6), \quad (110)$$

$$\begin{aligned} \boxed{q}_{ijk} = & \frac{34025}{48384}q_{ijk} + \frac{47477}{967680}q_{ijk}^{\Sigma 100} - \frac{2291}{483840}q_{ijk}^{\Sigma 200} + \frac{367}{967680}q_{ijk}^{\Sigma 300} \\ & + \frac{89}{34560}q_{ijk}^{\Sigma 110} - \frac{17}{138240}q_{ijk}^{\Sigma 210} + \frac{1}{13824}q_{ijk}^{\Sigma 111} + \mathcal{O}(h^8), \end{aligned} \quad (111)$$

$$\begin{aligned} \boxed{q}_{ijk} = & \frac{53802803}{77414400}q_{ijk} + \frac{2939507}{58060800}q_{ijk}^{\Sigma 100} - \frac{138211}{23224320}q_{ijk}^{\Sigma 200} + \frac{15403}{19353600}q_{ijk}^{\Sigma 300} \\ & - \frac{27859}{464486400}q_{ijk}^{\Sigma 400} + \frac{5581}{1814400}q_{ijk}^{\Sigma 110} - \frac{4691}{19353600}q_{ijk}^{\Sigma 210} + \frac{367}{23224320}q_{ijk}^{\Sigma 310} \\ & + \frac{289}{33177600}q_{ijk}^{\Sigma 220} + \frac{37}{276480}q_{ijk}^{\Sigma 111} - \frac{17}{3317760}q_{ijk}^{\Sigma 211} + \mathcal{O}(h^{10}). \end{aligned} \quad (112)$$

A.4 Formulas for area-averages/line-averages \leftrightarrow point values transformations

The 2D transformation formulas (area-average \leftrightarrow point values) are obtained by projecting the 3D formulas on a plane. All the terms with a subscript $(i \pm \alpha, j \pm \beta, k \pm \gamma)$ are replaced by terms with a subscript $(i \pm \alpha, j \pm \beta)$. After rearrangement of the terms this gives the formulas presented in section 3.2.2, which are not repeated here.

Projecting these formulas again on a line (that is, the subscripts $(i \pm \alpha, j \pm \beta)$ become $(i \pm \alpha)$, one obtains line-average \leftrightarrow point value transformations, useful e.g. when solving 2D problems:

$$q_i = \frac{x}{\bar{q}_i} + \mathcal{O}(\Delta x^2) \quad (113)$$

$$q_i = \frac{13}{12}\frac{x}{\bar{q}_i} - \frac{1}{24}\frac{x\Sigma 1}{\bar{q}_i} + \mathcal{O}(\Delta x^4) \quad (114)$$

$$q_i = \frac{1067}{960}\frac{x}{\bar{q}_i} - \frac{29}{480}\frac{x\Sigma 1}{\bar{q}_i} + \frac{3}{640}\frac{x\Sigma 2}{\bar{q}_i} + \mathcal{O}(\Delta x^6) \quad (115)$$

$$q_i = \frac{30251}{26880}\frac{x}{\bar{q}_i} - \frac{7621}{107520}\frac{x\Sigma 1}{\bar{q}_i} + \frac{159}{17920}\frac{x\Sigma 2}{\bar{q}_i} - \frac{5}{7168}\frac{x\Sigma 3}{\bar{q}_i} + \mathcal{O}(\Delta x^8) \quad (116)$$

$$q_i = \frac{5851067}{5160960}\frac{x}{\bar{q}_i} - \frac{100027}{1290240}\frac{x\Sigma 1}{\bar{q}_i} + \frac{31471}{2580480}\frac{x\Sigma 2}{\bar{q}_i} - \frac{425}{258048}\frac{x\Sigma 3}{\bar{q}_i} + \frac{35}{294912}\frac{x\Sigma 4}{\bar{q}_i} + \mathcal{O}(\Delta x^{10}) \quad (117)$$

$$\frac{x}{\bar{q}_i} = q_i + \mathcal{O}(\Delta x^2) \quad (118)$$

$$\frac{x}{\bar{q}_i} = \frac{11}{12}q_i + \frac{1}{24}q_i^{\Sigma 1} + \mathcal{O}(\Delta x^4) \quad (119)$$

$$\frac{x}{\bar{q}_i} = \frac{863}{960}q_i + \frac{77}{1440}q_i^{\Sigma 1} - \frac{17}{5760}q_i^{\Sigma 2} + \mathcal{O}(\Delta x^6) \quad (120)$$

$$\frac{x}{\bar{q}_i} = \frac{215641}{241920}q_i + \frac{6361}{107520}q_i^{\Sigma 1} - \frac{281}{53760}q_i^{\Sigma 2} + \frac{367}{967680}q_i^{\Sigma 3} + \mathcal{O}(\Delta x^8) \quad (121)$$

$$\frac{x}{\bar{q}_i} = \frac{41208059}{46448640}q_i + \frac{3629953}{58060800}q_i^{\Sigma 1} - \frac{801973}{116121600}q_i^{\Sigma 2} + \frac{49879}{58060800}q_i^{\Sigma 3} - \frac{27859}{464486400}q_i^{\Sigma 4} + \mathcal{O}(\Delta x^{10}) \quad (122)$$

References

- [1] P. L. Roe, Approximate Riemann solvers, parameter vectors, and difference schemes, Journal of Computational Physics 43 (1981) 357–372. doi:10.1016/0021-9991(81)90128-5.
- [2] E. F. Toro, M. Spruce, W. Speares, Restoration of the contact surface in the HLL-Riemann solver, Shock Waves 4 (1994) 25–34. doi:10.1007/BF01414629.
- [3] K. G. Powell, An approximate Riemann solver for magnetohydrodynamics, Upwind and High-Resolution Schemes (1997) 570–583 doi:10.1007/978-3-642-60543-7_23.

- [4] E. F. Toro, *Riemann Solvers and Numerical Methods for Fluid Dynamics*, Springer Berlin Heidelberg, 2009. doi:10.1007/b79761.
- [5] F. Miczek, F. K. Röpké, P. V. Edelmann, *Astronomy and Astrophysics* doi:10.1051/0004-6361/201425059.
- [6] T. Minoshima, T. Miyoshi, A low-dissipation HLLD approximate Riemann solver for a very wide range of Mach numbers, *Journal of Computational Physics* 446 (2021) 110639. doi:10.1016/J.JCP.2021.110639.
- [7] P. S. Verma, J.-M. Teissier, O. Henze, W.-C. Müller, Fourth-order accurate finite-volume CWENO scheme for astrophysical MHD problems, *Monthly Notices of the Royal Astronomical Society* 482 (2019) 416–437. doi:10.1093/mnras/sty2641.
- [8] P. McCorquodale, P. Colella, A high-order finite-volume method for conservation laws on locally refined grids, *Communications in Applied Mathematics and Computational Science* 6 (2011) 1–25. doi:10.2140/camcos.2011.6.1.
- [9] P. Buchmüller, C. Helzel, Improved accuracy of high-order WENO finite volume methods on cartesian grids, *Journal of Scientific Computing* 61 (2014) 343–368. doi:10.1007/S10915-014-9825-1.
- [10] J. N. de la Rosa, C.-D. Munz, XTROEM-FV: a new code for computational astrophysics based on very high order finite-volume methods – I. magnetohydrodynamics, *Monthly Notices of the Royal Astronomical Society* 455 (2016) 3458–3479. doi:10.1093/mnras/stv2531.
- [11] D. S. Balsara, T. Amano, S. Garain, J. Kim, A high-order relativistic two-fluid electrodynamic scheme with consistent reconstruction of electromagnetic fields and a multidimensional Riemann solver for electromagnetism, *Journal of Computational Physics* 318 (2016) 169–200. doi:10.1016/J.JCP.2016.05.006.
- [12] K. Wu, C. W. Shu, Provably positive high-order schemes for ideal magnetohydrodynamics: analysis on general meshes, *Numerische Mathematik* 142 (2019) 995–1047. doi:10.1007/S00211-019-01042-W.
- [13] C. R. Evans, J. F. Hawley, Simulation of magnetohydrodynamic flows - a constrained transport method, *The Astrophysical Journal* 332 (1988) 659. doi:10.1086/166684.
- [14] U. Ziegler, A central-constrained transport scheme for ideal magnetohydrodynamics, *Journal of Computational Physics* 196 (2004) 393–416. doi:10.1016/J.JCP.2003.11.003.
- [15] D. S. Balsara, C. Meyer, M. Dumbser, H. Du, Z. Xu, Efficient implementation of ADER schemes for Euler and magnetohydrodynamical flows on structured meshes – speed comparisons with Runge–Kutta methods, *Journal of Computational Physics* 235 (2013) 934–969. doi:10.1016/J.JCP.2012.04.051.
- [16] P. Londrillo, L. D. Zanna, High-order upwind schemes for multidimensional magnetohydrodynamics, *The Astrophysical Journal* 530 (2000) 508–524. doi:10.1086/308344.
- [17] A. Harten, B. Engquist, S. Osher, S. R. Chakravarthy, Uniformly high order accurate essentially non-oscillatory schemes, III, *Journal of Computational Physics* 71 (1987) 231–303. doi:10.1016/0021-9991(87)90031-3.
- [18] X. D. Liu, O. S. C. T, Weighted essentially non-oscillatory schemes, *Journal of Computational Physics* 115 (1994) 200–212. doi:10.1006/JCPH.1994.1187.
- [19] G. S. Jiang, C. W. Shu, Efficient implementation of weighted ENO schemes, *Journal of Computational Physics* 126 (1996) 202–228. doi:10.1006/JCPH.1996.0130.
- [20] C.-W. Shu, Essentially non-oscillatory and weighted essentially non-oscillatory schemes for hyperbolic conservation laws, ICASE Report 97-65 (1997).
URL <https://ntrs.nasa.gov/citations/19980007543>
- [21] D. S. Balsara, C. W. Shu, Monotonicity preserving weighted essentially non-oscillatory schemes with increasingly high order of accuracy, *Journal of Computational Physics* 160 (2000) 405–452. doi:10.1006/JCPH.2000.6443.
- [22] G. A. Gerolymos, D. Sénéchal, I. Vallet, Very-high-order WENO schemes, *Journal of Computational Physics* 228 (2009) 8481–8524. doi:10.1016/J.JCP.2009.07.039.
- [23] D. Levy, G. Puppo, G. Russo, Central WENO schemes for hyperbolic systems of conservation laws, *ESAIM: Mathematical Modelling and Numerical Analysis* 33 (1999) 547–571. doi:10.1051/M2AN:1999152.

- [24] J. Balbás, E. Tadmor, Nonoscillatory central schemes for one- and two-dimensional magnetohydrodynamics equations. II: High-order semidiscrete schemes, *SIAM Journal on Scientific Computing* 28 (2006) 533–560. doi:10.1137/040610246.
- [25] V. V. Rusanov, The calculation of the interaction of non-stationary shock waves and obstacles, *USSR Computational Mathematics and Mathematical Physics* 1 (1962) 304–320. doi:10.1016/0041-5553(62)90062-9.
- [26] C. W. Shu, S. Osher, Efficient implementation of essentially non-oscillatory shock-capturing schemes, II, *Journal of Computational Physics* 83 (1989) 32–78. doi:10.1016/0021-9991(89)90222-2.
- [27] D. S. Balsara, Multidimensional HLLC Riemann solver: Application to Euler and magnetohydrodynamic flows, *Journal of Computational Physics* 229 (2010) 1970–1993. doi:10.1016/J.JCP.2009.11.018.
- [28] D. S. Balsara, B. Nkonga, Multidimensional riemann problem with self-similar internal structure – part III – a multidimensional analogue of the HLLC Riemann solver for conservative hyperbolic systems, *Journal of Computational Physics* 346 (2017) 25–48. doi:10.1016/J.JCP.2017.05.038.
- [29] P. Londrillo, L. D. Zanna, On the divergence-free condition in Godunov-type schemes for ideal magnetohydrodynamics: the upwind constrained transport method, *Journal of Computational Physics* 195 (2004) 17–48. doi:10.1016/J.JCP.2003.09.016.
- [30] M. M. Low, The energy dissipation rate of supersonic, magnetohydrodynamic turbulence in molecular clouds, *The Astrophysical Journal* 524 (1999) 169–178. doi:10.1086/307784.
- [31] A. G. Kritsuk, R. Wagner, M. L. Norman, Energy cascade and scaling in supersonic isothermal turbulence, *Journal of Fluid Mechanics* 729 (2013) R1. doi:10.1017/JFM.2013.342.
- [32] H. Aluie, Scale decomposition in compressible turbulence, *Physica D: Nonlinear Phenomena* 247 (2013) 54–65. doi:10.1016/j.physd.2012.12.009.
- [33] S. Gottlieb, C.-W. Shu, Total variation diminishing Runge-Kutta schemes, *Mathematics of Computation* 67 (1998) 73–85. doi:10.1090/S0025-5718-98-00913-2.
- [34] S. Gottlieb, C. W. Shu, E. Tadmor, Strong stability-preserving high-order time discretization methods, *SIAM Review* 43 (2001) 89–112. doi:10.1137/S003614450036757X.
- [35] D. I. Ketcheson, Highly efficient strong stability-preserving Runge–Kutta methods with low-storage implementations, *SIAM Journal on Scientific Computing* 30 (2008) 2113–2136. doi:10.1137/07070485X.
- [36] J. F. Kraaijevanger, Contractivity of Runge-Kutta methods, *BIT Numerical Mathematics* 31 (1991) 482–528. doi:10.1007/BF01933264.
- [37] S. J. Ruuth, R. J. Spiteri, Two barriers on strong-stability-preserving time discretization methods, *Journal of Scientific Computing* 17 (2002) 211–220. doi:10.1023/A:1015156832269.
- [38] D. I. Ketcheson, S. Gottlieb, C. B. Macdonald, Strong stability preserving two-step Runge–Kutta methods, *SIAM Journal on Numerical Analysis* 49 (2011) 2618–2639. doi:10.1137/10080960X.
- [39] C. Bresten, S. Gottlieb, Z. Grant, D. Higgs, D. I. Ketcheson, A. Németh, Explicit strong stability preserving multistep Runge–Kutta methods, *Mathematics of Computation* 86 (2017) 747–769. doi:10.1090/mcom/3115.
- [40] S. Gottlieb, D. Higgs, D. I. Ketcheson, Multistep multistage (MSRK) methods.
URL <http://www.sspsite.org/msrk.html>
- [41] D. S. Balsara, Second-order-accurate schemes for magnetohydrodynamics with divergence-free reconstruction, *The Astrophysical Journal Supplement Series* 151 (2004) 149–184. doi:10.1086/381377.
- [42] A. Mignone, P. Tzeferacos, G. Bodo, High-order conservative finite difference GLM–MHD schemes for cell-centered MHD, *Journal of Computational Physics* 229 (2010) 5896–5920. doi:10.1016/J.JCP.2010.04.013.
- [43] G. Leidi, C. Birke, R. Andrassy, J. Higl, P. V. Edelmann, G. Wiest, C. Klingenberg, F. K. Röpke, *Astronomy and Astrophysics* doi:10.1051/0004-6361/202244665.

- [44] P. Colella, P. R. Woodward, The piecewise parabolic method (PPM) for gas-dynamical simulations, *Journal of Computational Physics* 54 (1984) 174–201. doi:10.1016/0021-9991(84)90143-8.
- [45] D. S. Balsara, Self-adjusting, positivity preserving high order schemes for hydrodynamics and magnetohydrodynamics, *Journal of Computational Physics* 231 (2012) 7504–7517. doi:10.1016/J.JCP.2012.01.032.

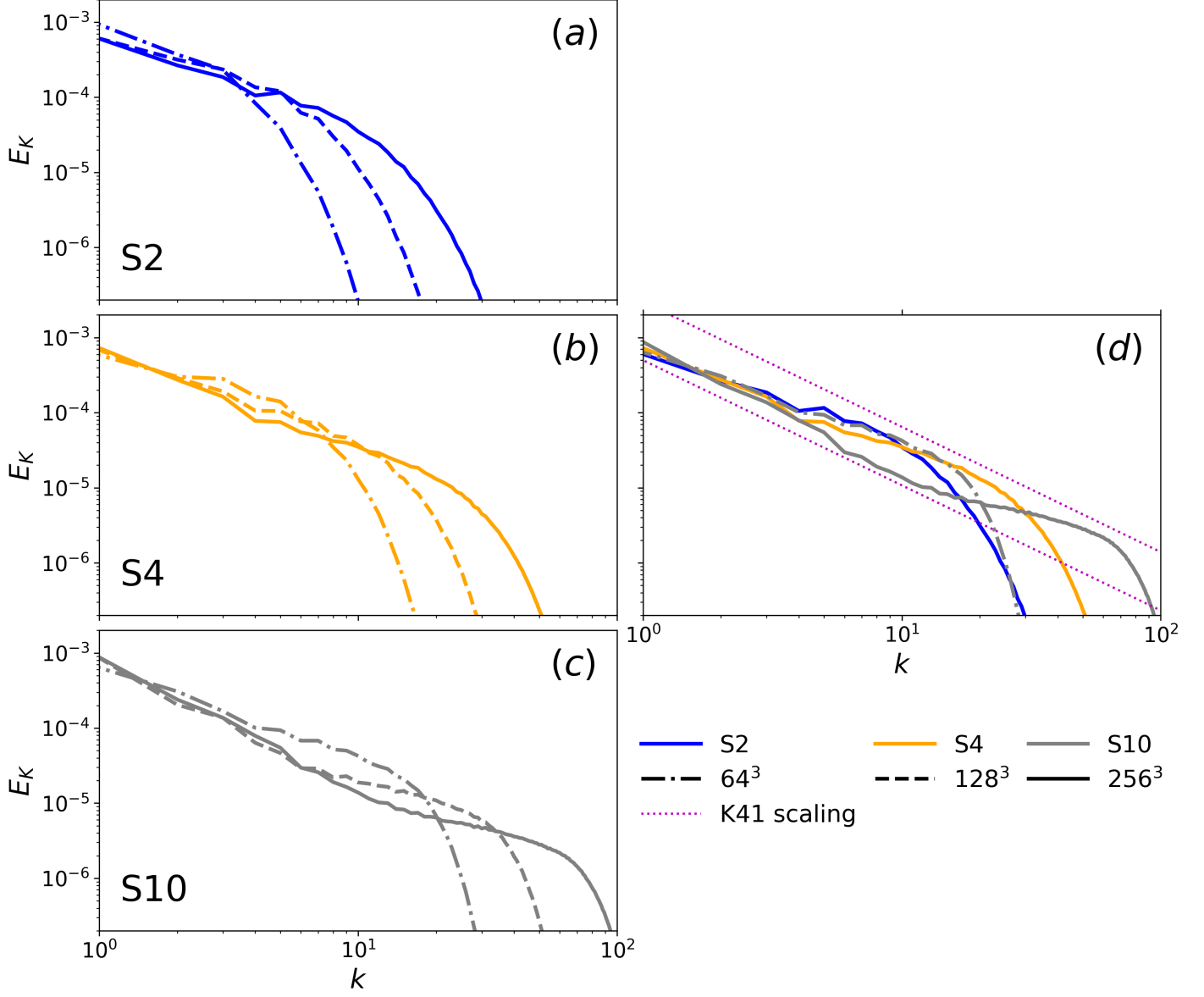


Figure 14: Hydrodynamic turbulent statistically stationary state: velocity power spectra for the schemes S2, S4 and S10 at resolutions 64^3 , 128^3 and 256^3 .

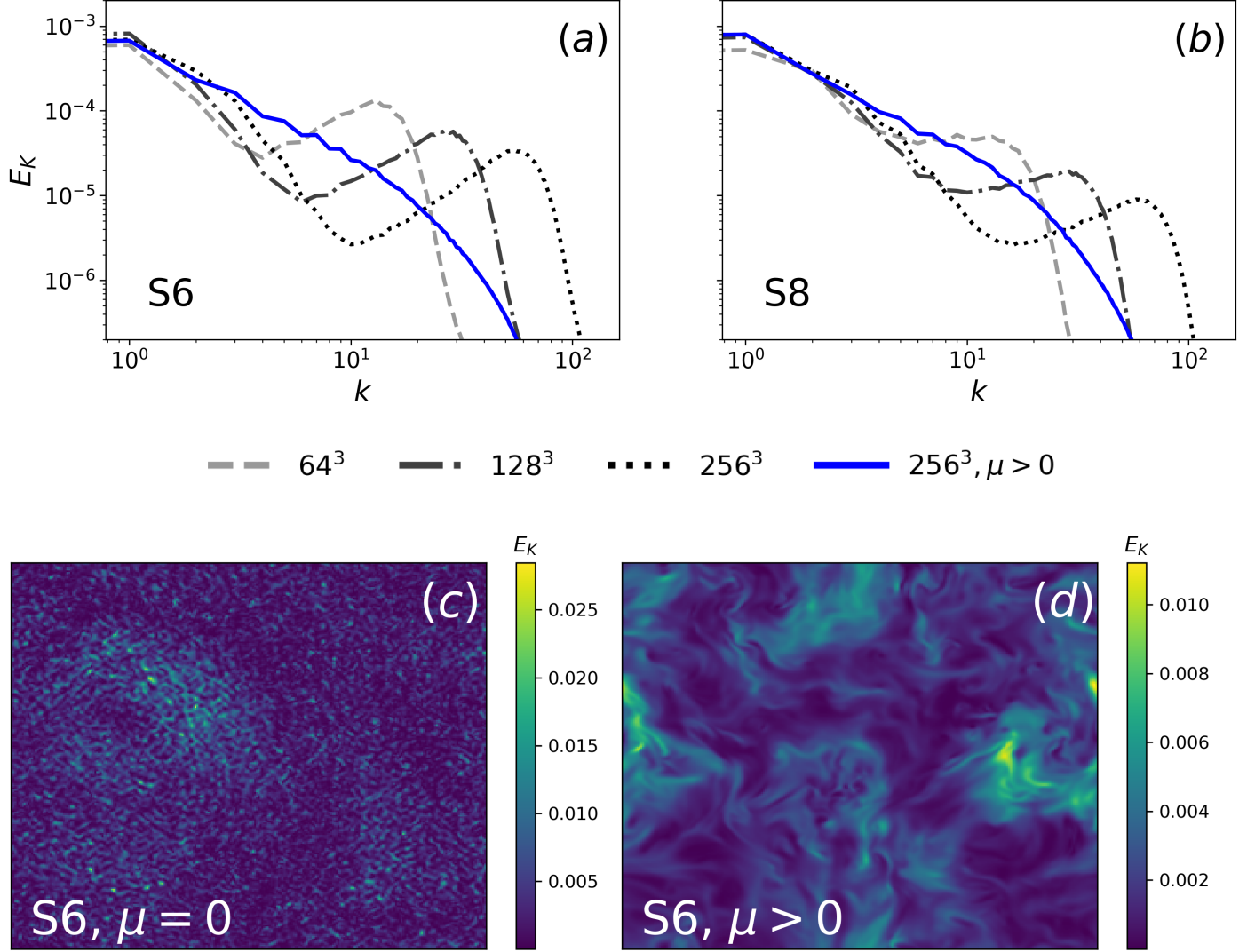


Figure 15: Hydrodynamic turbulent statistically stationary state: (a, b) velocity power spectra for the S6 and S8 schemes, (c, d) slices of the kinetic energy for the S6 scheme at resolution 256^3 , without and with viscosity respectively.

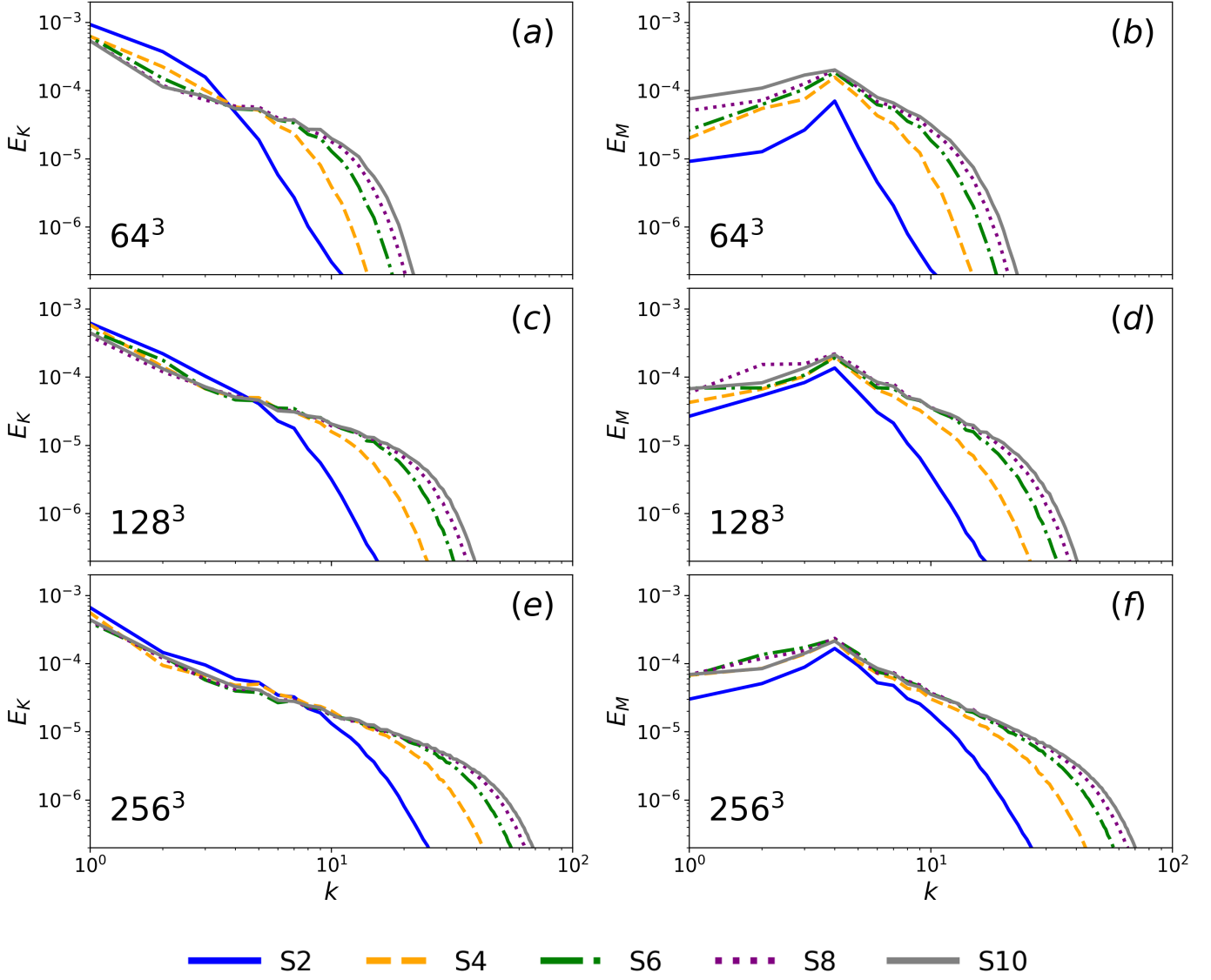


Figure 16: Fourier power spectra of the velocity (left) and magnetic fields (right) during the MHD turbulent statistically stationary state at different resolutions.